Malaysian Journal of Chemistry, 2026, Vol. 28(2), 347-376
(Special Issue: *1st International Conference on Chemical and Energy Engineering 2025, ICChEE2025*)

Green Materials and Approach in Focus: Enhancing Catalytic Activity of Hydrogen Fuel Cells – A State of an Art Review

Zargham Shahid Cheema and Juhana Jaafar*
Advanced Membrane Technology Research Centre (AMTEC),
Faculty of Chemical and Energy Engineering, Universiti Teknologi Malaysia, 81310 Johor Bahru,
Johor, Malaysia
*Corresponding author (e-mail: juhana@utm.my)

Green and sustainable catalyst design is critical to scaling hydrogen fuel-cell technologies beyond niche applications. This review examines recent advances in majorly four classes of green electrocatalysts: carbon-based biomass derivatives, hybrid & non-precious metals (Fe, Co, Ni), bio-inspired systems, and metal-organic frameworks (MOFs) as sustainable alternatives to mitigate these issues. Carbon-based catalysts leverage renewable biomass feedstocks and low-energy pyrolysis, reducing dependence on fossil-derived precursors. Hybrid & non-precious metals address Platinum group metal (PGM) scarcity by utilizing Earth-abundant elements, while bio-inspired designs mimic natural enzymatic efficiency through biodegradable, low-toxicity frameworks. MOFs, tailored with eco-friendly linkers and solvent-free synthesis, offer tunable active sites without heavy metals. Key mechanisms such as electron transfer, adsorption dynamics, and reaction kinetics are discussed to elucidate catalytic enhancement strategies. Despite their potential, challenges persist in optimizing cost-effective scalability, minimizing environmental footprints during synthesis, and ensuring long-term catalytic stability. By prioritizing renewability, energy efficiency, and reduced toxicity, green materials present a pathway to overcome the limitations of conventional catalysts. Future efforts must focus on advancing synthesis techniques, enhancing material recyclability, and aligning scalable production with circular economy principles to realize eco-efficient hydrogen fuel cell technologies.

Keywords: Hydrogen fuel cells, Green catalytic materials, Hybrid & non-precious metals (Fe, Co, Ni), Bio-inspired catalysts, Metal-organic frameworks (MOFs)

Received: July 2025; Accepted: January 2026

Hydrogen fuel cells are increasingly viewed as a cornerstone of a low-carbon energy economy, since they convert hydrogen into electricity with water as the only byproduct. However, widespread adoption has been limited by the high cost and scarcity of traditional platinum-group metal (PGM) catalysts. For example, platinum and iridium the standard catalysts fuel cells are extremely valuable and subject to supply constraints. As a result, fuel-cell stacks remain expensive and heavily dependent on mined PGMs. In this context, research is intensifying on “green” catalyst strategies that exploit earth-abundant, renewable, or waste-derived materials. These approaches aim to reduce reliance on costly metals, minimize waste, and align fuel cell technology with circular-economy principles. By converting waste biomass and abundant elements into high-performance catalysts, these green approaches address both economic and environmental challenges. Key strategies include optimizing electron-transfer pathways, adsorption/desorption energies, and active-site geometry through structural tuning. Nonetheless, hurdles remain: many non-precious catalysts still lag behind Pt benchmarks in intrinsic activity and long-term durability, and scalable synthesis methods must minimize energy use and toxic reagents. Future research must therefore integrate techno-economic and life-cycle analyses, advancing synthesis and recycling methods to align hydrogen fuel cell development with sustainable, circular-economy principles. By emphasizing renewable feedstocks, energy-efficient processing, and low toxicity in catalyst design, these green strategies hold promise to overcome the current limitations of fuel cell technology. This review highlights sustainable catalyst innovations for hydrogen fuel cells, focusing on green materials such as biomass-derived carbons, earth-abundant metals, bio-inspired systems, and eco-friendly MOFs, while addressing their mechanisms, advantages, challenges, and future directions toward scalable, low-toxicity, and high-performance clean energy solutions.

Carbon Based Biomass Derivatives

Carbon-based biomass-derived catalysts converted from biomass based & waste feedstocks (e.g., agricultural or forestry residues), pyrolyzed biomass yields high-surface-area carbon supports. Such

---

†Paper presented at the 1st International Conference on Chemical and Energy Engineering 2025 (ICChEE2025)

materials are renewable and inexpensive, offering a cost-effective alternative to fossil-derived carbons Heteroatom doping (N, P, S, etc.) during low-energy pyrolysis can introduce catalytic active sites (for ORR/HER) and improve conductivity.

Biomass-derived carbon materials were reviewed as heterogeneous catalysts for hydrogen evolution (HER) and oxygen reduction reactions (ORR), targeting low-cost substitutes for platinum. They choose bio-waste precursors (soybeans, plum blossom, spinach, chitosan, fish waste) because their derived carbons offer high surface area, tunable porosity, hydrophobicity and chemical inertness. Their synthesis strategies include chemical activation of biomass with $ZnCl_2$, KOH, NaOH or H_3PO_4 to produce activated carbons; pyrolysis and heteroatom doping (N, P, S) of starches and agricultural residues; multi-step CNT production from chicken feathers via Ni_3S_2-coated CNF precursors; hydrothermal CNS fabrication from areca nut kernels; and oxidative/sulfonation treatments to introduce Brønsted acidic groups. Heteroatom sites (graphitic and pyridinic N) and defect sites in these biomass-derived carbons create active centers for proton and oxygen adsorption, while bifunctional catalysis, synergistic dopant interactions, and tuned surface acidity/basicity enhance intermediate binding, charge transfer, and overall kinetics. As a result,

> MoSoy/Graphene achieves HER $\eta_{10} \approx 85$ mV with > 500 h acidic stability, N-doped plum blossom carbon delivers ORR $E_{1/2} = 0.82$ V at 5.96 mA cm^{-2} with 91.2 % retention over 50 000 s, and chitosan-Co NCNT reaches ORR $E_{1/2} = 0.80$ V.

MoSoy achieves HER overpotential $\eta_{10} \approx$ 85 mV with > 500 h durability in acid, and N-doped plum blossom carbon reaches ORR half-wave potentials within 40 mV of Pt/C, maintaining > 90 % current retention over 14 h. Biomass-derived catalysts are low-cost, abundant, CO_2-neutral, and recyclable PC-700 retains activity after eight cycles and nano-Pd@RAGC after ≥ 10 runs. Challenges include enhancing acidic-media activity without raising GWP, stabilizing doped carbons in harsh electrolytes, and developing continuous electrochemical reactors; future work should integrate earth-abundant catalysts into membrane electrode assemblies and apply DFT and in situ spectroscopy to illuminate active-site structures [1]. Conversion of waste humins via hydrothermal carbonization into non-graphitic powder, press into binder-free pellets, and nitrogen-dope to modulate electronic structure.

In alkaline 0.1 M KOH, continuous carbon oxidation (onset 1.02 V_RHE) generates H_2 at the cathode more efficiently than OER (1.52 V_RHE). Nitrogen-doped pellets reach ~80% catalytic OER contribution, boosting stability over 10 days.

Functional groups on carbon may trap iron impurities, but true metal-free performance stems from N-modulated work functions. These electrodes convert CO_2 back into biomass feedstocks, closing the carbon loop. Scaling to MW electrolyzers will need continuous biomass feeding and carbon recovery [2].

Figure 1. Biomass-derived carbon nanostructures (0D–3D) are being developed and applied as functional materials in fuel cells [3].

Biomass-derived carbon nanostructures such as spheres, fibres, tubes, and ribbons from precursors including chitosan, camphor leaf and bacterial cellulose, were synthesized using arc discharge, laser ablation, ionic liquid assisted chemical vapor deposition, hydrothermal pretreatment, and pyrolysis. In their approach, transition metals (Fe, Co, and Ni) nucleate graphitic frameworks while ionic liquids introduce heteroatoms and control morphology, producing quantum-confinement effects that enhance exciton dissociation, charge transport, and reduce recombination. Their biomass carbon tungsten nanohybrids accelerate triiodide reduction, and graphene-doped active layers boost exciton separation and thermal stability, yielding materials with high conductivity, large surface area and excellent catalyst anchoring for fuel-cell electrodes. Future work should focus on scaling ionic liquid CVD for large-area gas diffusion layers, integrating these nanomaterials into catalyst layers to optimize three-phase boundaries, quantifying ORR and HER performance, and establishing sustainable ionic liquid recycling [4]. Conversion of waste lignin, a high-carbon, heteroatom-rich pulp residue—into three nitrogen-doped porous carbons (N ELC, N ALC, N DLC) via enzymatic, alkaline, and dealkaline routes, annealing at 900 °C and acid washing to create mesoporous channels. Pyridinic N sites in these materials reduce O_2 adsorption barriers, while graphitic N boosts limiting current density, and the interconnected pore network speeds electron transfer and mass transport.

N ALC achieved an ORR half-wave potential ($E_{1/2}$) of 0.84 V (vs. RHE), onset at 0.96 V, BET area of 332.8 m^2/g, and I_D/I_G of 1.01, reaching ~95% of Pt/C performance. N ELC delivered $E_{1/2} = 0.82$ V and onset at 0.93 V with 55.8 m^2/g surface area, still exceeding 95% of Pt/C's half-wave potential.

Both catalysts showed stable voltammetric behavior over multiple cycles. By valorizing lignin into high-performance, low-cost ORR catalysts, this approach cuts environmental impact and material costs. Next steps include testing in membrane-electrode assemblies, evaluating long-term durability in full cells, and investigating co-doping strategies for further activity enhancements [5].Pt/HTC-Pyr catalyst was produced by depositing 1.8 ± 0.5 nm Pt nanoparticles via a microwave-assisted polyol method onto coconut-shell biochar prepared by hydrothermal carbonization below 300 °C followed by pyrolysis at 1100 °C to enlarge pores, remove surface groups and enhance conductivity.

In ORR the catalyst follows a four-electron pathway and delivers an onset potential of 0.94 V versus RHE (1.00 V for Pt/Vulcan), a half-wave potential of 0.80 V (0.90 V), a mass activity of 5.5 A gPt^{-1} (112.8 A gPt^{-1}) and an ECSA of 69 m^2 gPt^{-1} (69 m^2 gPt^{-1}), but it suffers 67 % ECSA loss after stress tests compared with 31 % for Pt/Vulcan. It's lower stability results from a more amorphous biochar support with fewer functional groups and reduced conductivity, although the agro-waste feedstock makes it environmentally sustainable and cost-effective. Future work should optimize graphitization and pore architecture, assess life-cycle impacts and explore oxidative post-treatments, heteroatom doping and integration into membrane-electrode assemblies to boost performance [6]. An N-doped bio carbon composite (N-BC@CNP-900) was produced by carbonizing enoki-mushroom biomass at 300 °C, milling it with commercial carbon nanoparticles, then pyrolyzing the mixture at 900 °C under N_2, leveraging enoki's > 31 wt % bioprotein content as a renewable nitrogen source.

During ORR, pyridinic-N and graphitic-N sites stabilize O_2 adsorption and facilitate electron donation into antibonding O_2 orbitals, while the CNP network promotes electron transport and prevents agglomeration. The catalyst achieves an onset potential of 0.94 V vs RHE (0.95 V for JM Pt/C), an electron transfer number of ~ 3.9 (4.0), a kinetic current of 21.7 mA cm^{-2}, a peak potential of 0.56 V in H_2SO_4, and shows negligible activity loss after 2000 cycles, demonstrating near-Pt performance in alkaline ORR.

Although mushroom-derived N-BC is low-cost, biodegradable and avoids harsh precursors, challenges remain in scaling uniform doping, reducing pyrolysis energy and extending performance into acidic media; future work should tune pyrolysis temperature for optimal N-species ratios, integrate the composite into 3D architectures to boost mass transport and perform life-cycle assessments of fungal feedstocks [7]. Waste coffee sludge was transformed into activated hydrochar via hydrothermal carbonization and KOH activation, yielding a graphitic, micro/mesoporous carbon with intrinsic N, O, and S heteroatoms. Such a support could enhance both HER and ORR catalysts by improving reactant diffusion and providing electron-rich adsorption sites; its high surface area (>1000 m^2 g^{-1}) and low resistance (R_ct ~11 Ω) suggest rapid kinetics and good catalyst utilization. The material's excellent supercapacitor stability implies robustness under cycling; leveraging ubiquitous coffee waste reduces landfill burden, though tailoring heteroatom content for specific fuel-cell reactions and assessing activity in electrochemical half-cells are needed [8].Aesculus turbinata seed biomass was converted into N/S-doped porous carbon via one-step pyrolysis, yielding a meso/microporous network with 2 at% N and 1 at% S. Pyridinic and graphitic nitrogen would catalyze ORR while sulfur sites could improve H_2 adsorption for HER, and the porous architecture would facilitate mass transport. Its high electrochemical stability over 10,000 charge discharge cycles predicts excellent durability in fuel-cell environments, and using seed waste offers a low-cost, sustainable route; further work should measure specific ORR/HER metrics and elucidate the synergistic role of dual heteroatoms [9]. Waste cigarette butts were converted into Fe-N-C ORR catalysts by pyrolyzing ball-milled filters at 450–900 °C, activating with KOH (4:1), acid-washing, then mixing with 10 wt % FePc and a final 600 °C pyrolysis—yielding cig_450 as the top performer. Fe–N_x moieties on high-surface-area carbons bind O_2 and direct it through either direct four-electron or 2×2-electron pathways; micropores host the active sites, mesopores facilitate reactant transport, and uniform Fe distribution lowers bond-breaking barriers.

In alkaline media cig_450's $E_{1/2}$ (0.85 V) rivals Pt/C and $n > 3.2$ confirms near-4e⁻ ORR, though J_lim falls 50–59 % after 2000 cycles due to Fe leaching. Valorizing zero-cost waste butt feedstock aligns with circular-economy goals and cuts PGM dependence; future work must stabilize Fe–Nx sites against leaching, explore co-dopants for durability, and validate performance in full FC stacks [10].

Table 1. ORR Performance of cig_450 Catalyst in Different Electrolytes.

Electrolyte	E_{on} (V vs. RHE)	$E_{1/2}$ (V vs. RHE)	n (electron number)
Acidic	0.88	0.68	3.6–4.0
Neutral	0.77	0.43	3.4–3.95
Alkaline	0.91	0.85	> 3.2

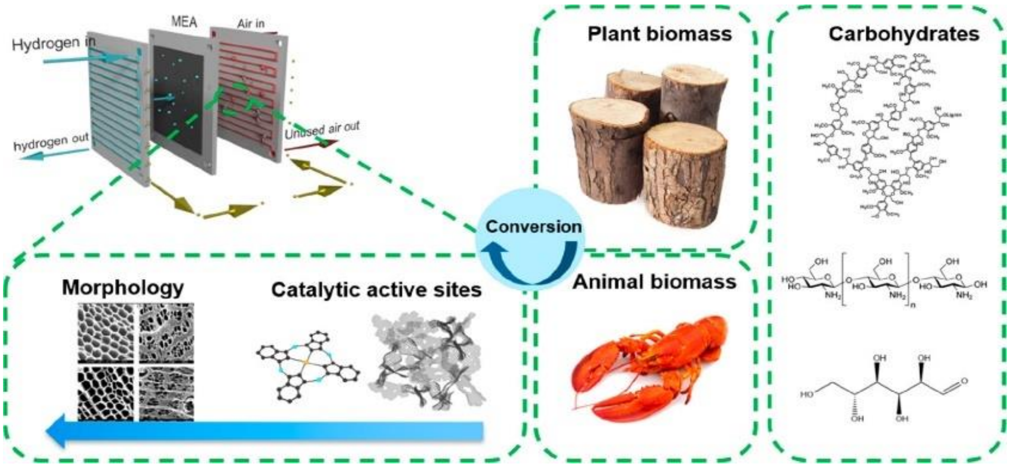

Figure 2. Schematic of biomass types and the active sites in the cathode side of the fuel cell. Figures added with permission from [11].

Table 2. Electrochemical Performance of ACF Samples.

Metric	Aqueous KOH	Aqueous H_2SO_4	Non-aqueous TEMA BF_4/PC	ORR Onset (S23)	Kinetic Current (P21)
Specific Capacitance ($F\cdot g^{-1}$)	205	155	127	—	—
ORR Onset Potential (V vs SHE)	—	—	—	−0.41 V	—
Kinetic Current ($A\cdot g^{-1}$)	—	—	—	—	~ 250
Electron Transfer Number	—	—	—	2 e⁻ (peroxide)	—
Stability	High (no decay)	High	High	—	—

Viscose fibers were converted into activated carbon fibers for ORR electrocatalysis by impregnating dried fibers in 4 % diammonium hydrogen phosphate for the P21 sample, which underwent 150 min CO_2 activation, or in 12 % ammonium sulfate for the S23 sample, which underwent 300 min activation, then carbonizing in N_2 at 850 °C for 20 min and activating with CO_2 at 850 °C. In ORR these ACFs form a Helmholtz double layer at the electrode–electrolyte interface; mesopores enable rapid ion transport, micropores provide high adsorption, and surface OH, COOH, N and P groups support pseudo faradaic redox and tune conductivity.

These ACFs deliver up to 205 $F \cdot g^{-1}$ capacitance and selective peroxide-pathway ORR with −0.41 V onset, illustrating their dual energy-storage and ORR catalytic roles. Renewable viscose and straightforward impregnation confer scalability and cost-effectiveness, and selective H_2O_2 formation adds value. Challenges include improving 4 e^- ORR selectivity for direct water production, demonstrating long-term fuel-cell cycling stability, standardizing ORR measurements, exploring multi-heteroatom co-doping (N,S,P), and scaling CO_2 activation economically[12].Biomass-derived carbon fibers (CFs) from rayon, lignin, glycerol and sugars as renewable, low-cost alternatives to fossil-based PAN CF were reviewed with the goal of reducing both cost and environmental impact. These biomass CFs exhibit high conductivity, hierarchical porosity, and tunable surface chemistry, which are critical for supporting ORR and HER catalysts by enhancing charge transfer, adsorption, and mass transport. When deployed as electrode supports, they can uniformly disperse active metal or metal oxide catalysts, improve electron conduction, and facilitate reactant and product transport; for example, lignin CFs cost $4–6 per pound compared with $10 for PAN CF, and producing them from waste polymers further lowers fossil dependency. Future work should improve CF conductivity and mechanical strength to match PAN levels, adopt greener stabilization and carbonization methods, ensure consistent feedstock quality, explore direct heteroatom doping for intrinsic catalytic activity and assess CF recyclability within a circular-economy framework [13]. Biomass-derived carbon nano catalysts were demonstrated, such as activated porous carbons, carbon nanotubes, carbon quantum dots, graphene derivatives, biochars and MOF-derived carbons, offer high electrical conductivity and large specific surface areas for rapid electron transport and maximal catalyst dispersion in PEM fuel cell electrodes. Surface sulfonic and carboxylic groups provide abundant anchoring sites for ORR catalysts and enhance oxygen adsorption; heteroatom doping (N, S, P) tailors electronic states to lower over potentials; CNT–metal oxide and CQD–semiconductor heterojunctions boost interfacial charge transfer, and MOF-derived carbons stabilize single-atom catalysts to increase active-site utilization and durability. These materials are produced by scalable, low-cost methods including chemical activation with H_3PO_4 or KOH, oxidative or sulfonation treatments and MOF pyrolysis using waste precursors, and they have proven performance in oxidation reactions with Pt/CNTs achieving 100 % HMF-to-FDCA conversion and CoSA/N@C doubling HMF oxidation activity compared with nanoparticle catalysts, making them directly transferable to ORR cathodes where Pt/CNTs could lower over potentials and improve mass transport. Future work should optimize support morphology for well-defined three-phase interfaces, develop metal-free ORR catalysts via heteroatom-doped biochar and validate long-term cycling stability in membrane-electrode assemblies [14].Waste-coffee-grounds carbons (WCG-C) were applied to supercapacitors and batteries, but their tunable porosity, graphitic domains, and heteroatom sites (pyridinic-N, pyrrolic-N, P) make them ideal metal-free ORR supports or catalysts in fuel-cell cathodes [15]. Nitrogen-doped carbons produced from nitrilotriacetic acid and $MgCO_3$ by sequential oxidation (350–500 °C) to remove amorphous domains and enrich pyridinic and graphitic N sites, followed by pyrolysis, confirming a uniform porous network optimized for catalysis.

In ORR the graphitic N sites facilitate four-electron transfer to water, pyridinic N lowers over-potentials by strong O_2 binding, and homogeneous pore structures expedite adsorption and diffusion. In 0.1 M KOH the Ox 500 P sample reaches an onset potential of 0.97 V, a half-wave potential of 0.85 V, an electron transfer number of ~3.6 and high corrosion resistance approaching the 0.99 V, $n = 4.0$ performance of 20 wt % Pt/C.

This green, scalable, Pt-free method uses earth-abundant carbon and nitrogen precursors, generates only water as a byproduct, and future efforts should focus on enhancing activity in acidic media, achieving industrial-scale uniformity of nitrogen speciation and defect densities, and expanding feedstocks to include agricultural waste [16]. Rice-husk-derived carbon nanomaterials were reported (CNTs, CDs, GQDs, CQDs, graphene) as catalyst supports. They chose rice husk because it is abundant, renewable agricultural waste rich in lignin, cellulose, and hemicellulose, enabling a “waste-to-riches” strategy that yields low-cost, high-surface-area CNMs with tunable porosity and defect sites ($ID/IG \approx 1–2$). These sp^2-rich networks promote rapid electron transfer through conductive pathways and strong adsorption of reactants on defect-laden surfaces; hierarchical pores facilitate fast mass transport, enhancing overall reaction kinetics. While they did not report ORR, OER, or HER metrics directly, their CNTs and GQDs would uniformly disperse active nanoparticles and promote efficient four-electron ORR pathways, and CDs/CQDs could boost proton conductivity at electrode interfaces. Stability under cycling wasn’t measured, but the inherent chemical inertness and robust carbon framework suggest good durability when employed in fuel [17]

Table 3. Studies demonstrate that catalytic graphitization of biomass-derived materials like coconut coir, protein whey, pine sawdust, and mangosteen peel using transition metal catalysts such as Ni, Fe, Co, and Mo leads to varying degrees of graphitization and surface areas. Higher SBET values, like those from whey (2536 m²/g) and sawdust (1366 m²/g), indicate improved porosity and active surface sites. If these materials are applied as electrode supports in fuel cells, their graphitized structure can significantly enhance electrochemical performance. High surface area and moderate graphitization (IG/ID ~1–1.2) favor better hydrogen evolution reaction (HER) and oxygen reduction reaction (ORR) kinetics due to improved electron transport and catalyst dispersion. Specifically, Fe and Co can promote ORR, while Ni-based carbon supports benefit HER activity. These bio-derived carbons thus show promising potential as cost-effective and sustainable electrode materials in fuel cell applications. environments.

Ref.	Source of Carbon + Catalyst(s)	Temp, Time, IG/ID	SBET (m²/g)
[18]	Coconut Coir + $NiCl_2$	1300°C, 3 h, 1.01 ± 0.04	51.61
[19]	Protein Whey + $Ni(NO_3)_2$	700°C, 1 h, 1.20	2536
[20]	Pine Sawdust + $Fe(NO_3)_3$	600–800°C, 5°C/min	112, 139
[21]	Sawdust + $NiCl_2$ & $(NH_4)_6Mo_7O_{26}$	750°C, 2 h, 1.05	1366
[22]	Dandelion Flower + K_2FeO_4	700°C, 2 h, 1.103	780.94
[23]	Mangosteen Peel + $CoCl_2$	800°C, 2 h, 1.26	1168
[24]	Miscanthus Grass + Fe(III), Co(II) Nitrates	500–900°C, 10°C/min	–
[25]	Palm Kernel Shell + Fe(III), Ni(III) Nitrates	1000°C	–

Ru/N-C produced from yeast for HER. Yeast was carbonized at 600 °C, $RuCl_3$-impregnated, and H_2-reduced at 400 °C to deposit Ru NPs on N-doped carbon. The N-C support disperses Ru and enhances electron transfer; Ru sites catalyze H^+ reduction with 0.20 V onset and 85 % stability over 60 h. Microbial biomass valorization and minimal Ru loading reduce cost; scaling fermentation and integrating bio electrochemical synthesis are promising next steps. HH AC 700 fabricated by annealing human hair ash/KOH mixtures at 700 °C for 2 h and washing, producing partially graphitized conductive domains with edge defects and mesopores that enhance H^+ adsorption and proton–electron transfer kinetics. This catalyst delivers a HER overpotential of 16 mV at 10 mA cm^{-2}, a Tafel slope of 51 mV dec^{-1} and 98 % retention after 1000 cycles, rivaling PGM catalysts in both activity and durability. The reuse of hair waste and moderate KOH activation offers a sustainable synthesis route, although reducing KOH effluent remains a challenge [26].

Synthesis method and functional descriptors were discussed with electrochemical performance and durability for selected biomass-derived and heteroatom-engineered carbon electrocatalysts.

Advanced carbon material precursors produced from walnut shells, peach, apricot and olive kernels using microwave-assisted pyrolysis. The resulting carbons contain less than 1 % ash and abundant oxygen functional groups that enhance adsorption and electron transfer when they support catalysts. Their combined microporous and mesoporous networks promote rapid mass transport and provide many active sites, while the oxygen groups improve proton adsorption and electron shuttling to boost kinetics. With BET surface areas of 114–295 m²/g, iodine indices up to 500 mg/g and stability up to 700 °C and in water, these materials valorize agricultural waste; future studies should integrate them into membrane–electrode assemblies and test long-term fuel-cell cycling to ensure scalable pore-architecture consistency [28]. A coral-like $Co@Co_3O_4/C$ nano hybrid was synthesized from a ZIF-67 precursor, yielding a magnetic, porous adsorbent with 554.8 m²/g surface area and 0.22 cm³/g pore volume. Cobalt sites act as non-precious active centers while the carbon matrix provides conductivity and π-π interactions for fast charge transfer. Although ORR and HER activities have not been reported, its pseudo-second-order adsorption kinetics for antibiotics suggest rapid surface reactions that could translate into high turnover frequencies in fuel-cell environments, and magnetic separation confirms robustness against leaching and fouling. The simple two-step synthesis and demonstrated reusability over four cycles highlight economic sustainability; future work must optimize cobalt loading and assess long-term stability under dynamic fuel-cell potentials [29]. Glucose based activated carbon nanospheres were synthesized (g ACNSs) via hydrothermal treatment of D (+)-glucose with polystyrene sulfonate and dual KOH activations. They chose D (+)-glucose for its low cost and renewable nature, producing CNSs with 2291 m^2/g surface area, ID/IG = 1.77, uniform 50 nm size, and 1–6 nm pores. The hierarchical micropores support physical adsorption in confined sites while defect rich surfaces enable chemical binding at sp bonded carbon sites, enhancing electron transfer and adsorption kinetics. Though their work reports hydrogen storage performance (5.04 wt % at 77 K/100 bar; 480 % uptake over 100 cycles), ORR/HER activity was not measured; however, g ACNSs' high surface area and defect networks would provide abundant nucleation centers for non-precious catalysts and efficient mass transport. Cycle stability in storage implies robust structural integrity adaptable to fuel cell cycling [30].

Bio-inspired

Bio-inspired catalytic systems replicate strategies found in natural enzymes, which achieve remarkable catalytic activity and selectivity under mild conditions. By mimicking active site architectures, cofactor arrangements, and microenvironments found in nature, researchers design synthetic catalysts that combine high efficiency with environmental compatibility. Such systems often use renewable, biodegradable, and low-toxicity components, aligning strongly with the goals of green chemistry and sustainable fuel cell technology.

Table 4. Summary of synthesis, key functional features, and electrochemical performance for selected biomass-derived and heteroatom-doped carbon electrocatalysts discussed by [27].

Precursor & Synthesis	Key Functional Features	Reaction	Overpotential (mV)	ORR Potentials (Onset / Half-Wave)	Limiting Current Density J_l (mA cm^{-2})	Tafel Slope / OER η_{10}	Stability & Durability
CNTs soaked in phytic acid, pyrolyzed at 900 °C, lightly oxidized	N,P sites tailor electronic structure for H^+ adsorption; thin nanosheets shorten charge paths	**HER**	167 (acidic), 440 (neutral), 304 (alkaline) **(mV @10 mA cm^{-2})**	–	–	– / –	< 5 % decay after 3 k cycles
Chitosan–Co^{2+} gel freeze-dried, pyrolyzed at 800 °C; $Co(NO_3)_2$ impregnation; annealed at 900 °C	Co–N_x moieties coordinate O_2; graphitic CNT walls enable fast electron paths; mesopores improve diffusion	**ORR**	–	– / 0.88 V	6.92	– / –	95 % retention after 10 k cycles
Seaweed hydrothermal carbonization at 200 °C for 12 h; wash, dry; KOH activation at 800 °C for 2 h; acid wash; anneal at 900 °C	Graphitic domains + oxygenated groups; hierarchical pores; edge defects & pyridinic N lower activation barriers; π-conjugation speeds ET	**ORR**	–	1.01 V / 0.83 V	–	– / –	< 5 % loss after 10 k cycles; unchanged after 24 h
L-lysine polymerized at 180 °C; carbonized at 800 °C under Ar; ammonia treated at 900 °C for 1 h; acid washed	Pyridinic & graphitic N in thin shells; hollow architecture minimizes diffusion lengths	**ORR/OER**	–	0.92 V / 0.80 V	–	– / 310 mV	5 % loss after 5 k cycles; < 10 % decay
Cysteine solution freeze-dried; pyrolyzed at 900 °C under Ar; H_2 treated at 700 °C	Pyridinic N & thiophenic S sites activate O_2; graphitic domains ensure fast ET; S-induced polar sites weaken O–O bonds	**ORR/OER**	–	– / –0.19 V vs SCE	–5.34	– / 0.69 V	< 5 % loss after 10 k cycles
Fructus azedarach shells + phosphoric acid + urea; carbonized at 800 °C for 2 h under N_2; KOH activated at 700 °C	Pyridinic N enhances O_2 adsorption; phosphate groups improve hydrophilicity & mass transport; graphitic networks afford conductivity	**ORR**	–	0.94 V / 0.84 V	–	119 mV dec^{-1} / –	90 % retention after 3 k cycles
Guanidine carbonate + glucose carbon; pyrolyzed at 900 °C; acid washed	Boron induces electron deficiency for O_2 adsorption; N dopants create active sites; 2D morphology shortens diffusion paths	**ORR**	–	0.94 V / 0.82 V	–	– / –	> 95 % retention after 5 k cycles

Programmable multi-enzyme scaffolds such as DNA origami, peptide tags, protein cages, polymersomes and virus-like particles as bio-inspired green materials for organizing redox enzymes on electrodes were reported. By mimicking cellular co-localization, these scaffolds enhance cascade efficiency and stability under mild conditions through proximity-driven substrate channeling, local cofactor pooling and enzyme stabilization via encapsulation or surface attachment. Although no direct HER, ORR or OER metrics are provided, loading these biodegradable, cell-free or microbially expressed scaffolds with electrocatalytic enzymes could lower overpotentials and increase current densities by maintaining high local enzyme concentrations and optimal orientations. Future challenges include achieving precise enzyme orientation for true electrocatalysis, scaling up synthetic-biology production and ensuring long-term operational stability under electrochemical bias [31].

Table 5. Comparative Overview of Bio-Inspired Electrocatalysts: Synthesis, Key Features, and Performance Metrics.

Ref.	Key Features	Catalyst / Complex	Reaction	Over Potential/onset	Tafel Slope (mV dec⁻¹)	j & Mass Activity	TOF (s⁻¹)	Stability & Durability
[32]	PDA film on Cu foil → carbonize at 800 °C → ~12 nm graphitic nanosheets with micropores; pyridinic/pyrrolic/graphitic N sites create H* adsorption centers;	C PDA	HER	68 mV (η @ 1 mA cm^{-2})	45	5 mA cm^{-2} @ –0.13 V;	–	> 80 % retained after 10 h
[33]	PDA + Fe/Co/Mn salts → solvothermal → pyrolysis @ 800 °C → $M–N_x$ sites adsorb O_2/OH^-; N-doped carbon matrix enhances electron transfer; n-electron: Co-NC 3.4, Fe-NC 3.7, Mn-NC 3.6	Co-NC; Fe-NC; Mn-NC	ORR / OER	Co-NC: 0.90 V ORR onset / 1.46 V OER η_{10} / ΔE 0.867 VFe-NC: 0.85 V / 1.60 V / 0.95 VMn-NC: 0.88 V / 1.58 V / 0.92 V	-	-	–	Co-NC: minimal loss after 10 k cyclesFe-NC/Mn-NC: stable
[34]	MWCNTs → $PyCO_2H$ functionalization → NiArg immobilization; electrostatic & π-cation anchoring; diffusion-limited $2e^-/2H^+$ HOR at Ni center; n-electron: not reported	$[NiII(P2CyN2Arg)_2]^{7+}$ (NiArg)	HOR			214 ± 20 (25 °C @ 0.4 V); 150 ± 20 (55 °C @ 0.1 V); 395 ± 30 (55 °C @ 0.4 V);mass activity: 83 A $mgNi^{-1}$	37 (25 °C); 64 (55 °C)	75 % after 100 CV scans96 % after 1 h chronoamperometry
[35]	AzPc (Fe/Co/Ni/Cu) on Ketjen Black via sonication & spray-coating; high ECSA; AEM functional groups modulate adsorption & proton transfer kinetics; n-electron: not reported	CoAzPc 4N; FeAzPc 4N; NiAzPc 4N; CuAzPc 4N	HER / AEMWE	CoAzPc 4N: 378 mV η_{10} (HER) / 2.11 V @ 1 A cm^{-2} (Fumasep)FeAzPc 4N: 408 mV / 2.02 V @ 1 A cm^{-2} (Sustainion®)Ni/Cu : not reported	CoAzPc: 120 FeAzPc: 208	-	–	stable 24 h at 200 mA cm^{-2}
[36]	Bis-imidazole/benzazole Co complexes via $Co(BF_4)_2$ or $Co(NO_3)_2$; ligand-embedded C–H relays facilitate proton-electron transfers; in situ Co deposits serve as active species; n-electron: not reported	$[Co(dmgBF_2)_2(H_2O)_2]$; Complex 19; $Co(HBBIM)_2^2$; $Co(HBBZM)_2^2$; $Co(HBBTM)_2^2$; $Co(HBMIMPh_2)_2^2$	HER	$[Co(dmgBF_2)_2(H_2O)_2]$: 100 mV @ pH<4.5Complex 19: 80 mV @ pH 7$Co(HBBIM)_2^2$: 610 mV$Co(HBBZM)_2^2$: 580 mV$Co(HBBTM)_2^2$: 490 mV$Co(HBMIMPh_2)_2^2$: 590 mV	-	-	$Co(HBBIM)_2^2$: 15$Co(HBBZM)_2^2$: 28$Co(HBBTM)_2^2$: 25$Co(HBMIMPh_2)_2^2$: 125	$[Co(dmgBF_2)_2]$: 16 hComplex 19: 20 h

A hybrid 3D nanocapsule featuring Fe single atoms embedded in an N-doped carbon shell and Au nanoparticles on the outer surface, spatially segregating peroxidase- and oxidase-like sites to mimic eukaryotic organelles and prevent active-site interference. They hydrothermally synthesize peanut-shaped α-Fe_2O_3 cores, coat them with polydopamine and anneal under argon to convert the shell into N-doped carbon trapping Fe atoms, then acid-leach residual oxides and uniformly load ~3.6 nm Au nanoparticles on the exterior. Proximity-facilitated H_2O_2 transfer reduces the DFT-calculated OH* protonation barrier from +0.16 eV to –0.26 eV while distinct inner and outer sites optimize adsorption kinetics. The Fe_1@Au NPs system delivers a 9.8-fold cascade enhancement versus mixed catalysts, 52.29 U mg^{-1} specific activity, a 0.13 µM detection limit and stable recyclability over at least 10 cycles; future work should adapt this core–shell concept to HER/ORR electrocatalysis, replace Au with less costly metals, integrate the nanocapsules into membrane-electrode assemblies and assess long-term structural durability under repeated redox cycling [37]. [FeFe] hydrogenase CpI and MoFe nitrogenase as bio-electrocatalysts were explored for green hydrogen fuel cells, reporting that CpI on nano-ITO electrodes delivers > 8 mA cm^{-2} H_2 evolution with ≈ 100 % Faradaic efficiency and retains ~ 94 % activity after 120 h. Photoexcited CdS-mediated electron delivery to MoFe achieves NH_3 production at 63 % of native ATP-driven rates, while formate dehydrogenase and formylmethanofuran dehydrogenase reduce CO_2 with near-perfect and 100 % Faradaic efficiencies, respectively. Electron transfer occurs via DET or MET under Marcus-type kinetics, and immobilization on transparent conductive oxides enhances both charge injection and operational stability. These systems leverage mild conditions and abundant metals for sustainable catalysis, yet O_2 sensitivity, large-scale enzyme production and electrode designs that maximize loading without compromising durability remain key hurdles. [38].

Both natural hydrogenases and bio-inspired molecular mimics were reviewed for H_2 fuel-cell applications, showing that FFH embedded in redox-polymer films achieves 1.16 V open-circuit voltage in H_2/O_2 biofuel cells and thermostable NFH bio anodes operate efficiently at 40–80 °C on nanotube-modified carbon felt.

Small-molecule "Hangman" porphyrins and peptide-based catalysts reach HER turnover numbers exceeding 230 000 at over potentials as low as 520 mV and maintain activity for up to 1.3 h. Electron transfer in these bio-fuel cells relies on direct wiring via redox polymers or carbon nanotubes to minimize activation losses, while pendant amines facilitate proton-coupled electron transfer in mimics.

Their mild operational conditions and use of abundant metals confer environmental and economic benefits, though long-term biomolecule stability under cycling and scalable peptide production remain significant challenges, motivating future work on covalent immobilization and fully protein-based membrane electrode assemblies[39]. An O_2-resistant [Fe Fe] hydrogenase, CbA5H was engineered by exploiting its Cys367 "safety cap" to reversibly protect the H-cluster under aerobic conditions and achieve an intrinsic $k_{kat} \approx 10^4\ s^{-1}$; an A419S variant further boosts k_{kat} above $10^4\ s^{-1}$ while maintaining reversible protection. Proton and electron transfer are tuned by a flexible TSC loop that regulates substrate access, and electrode immobilization leverages CbA5H's intrinsic O_2 tolerance to sustain stable H_2-oxidation currents in biofuel cells. As a protein catalyst operating at ambient conditions, CbA5H eliminates rare metals and advances economic and environmental sustainability. Future work must optimize electrode interfaces for maximal enzyme loading and develop chimeric "molecular Lego" assemblies for multi-step cascade fuel-cell reactions [40]. Bacterial synthesis of metal and metalloid nanoparticles from CuO and Fe_3O_4 to Pd and Pt as green catalysts were examined, harnessing enzyme systems (e.g., nitrate reductase, cytochrome c) to reduce ions under mild conditions and form extracellular NPs capped by proteins for stability. Although no ORR/OER metrics are reported, these biogenic NPs exhibit high surface-to-volume ratios and stable capping layers that would facilitate rapid electron transfer and abundant adsorption sites;

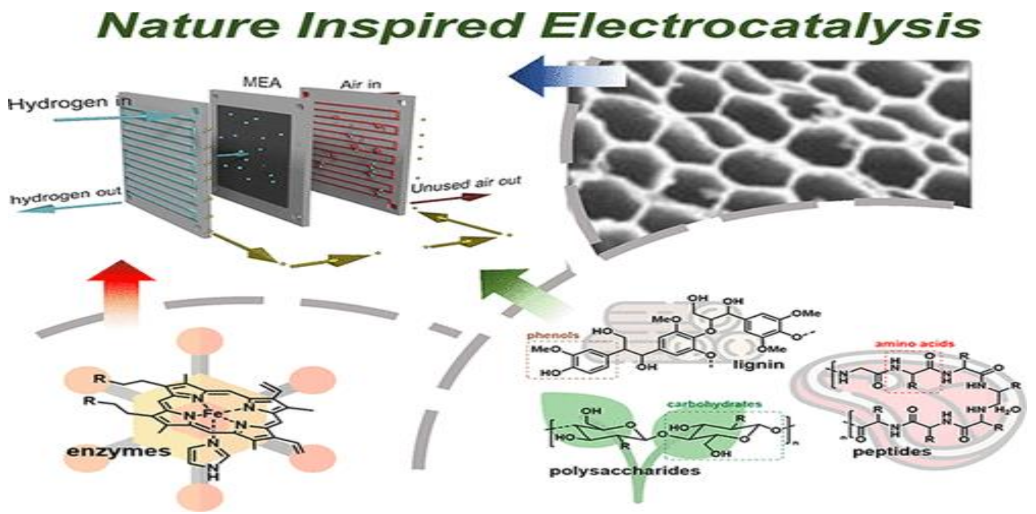

Figure 3. Nature-inspired electrocatalysis for hydrogen fuel cells.Biomolecular building blocks (polysaccharides, lignin/phenolics, peptides/amino acids) and enzyme-inspired motifs (e.g., Fe–N–C-like centers) guide the design of biomimetic catalysts that enhance active-site dispersion, mass transport, and catalytic selectivity/stability in fuel-cell electrodes [42].

Pd NPs outperform chemically synthesized analogs in dechlorination by 30×, hinting at superior catalytic kinetics, while Cu and Fe oxides offer cost-effective Pt alternatives. These NPs are readily recoverable and maintain activity over multiple cycles, aligning with circular-economy goals through low-energy, waste-valorizing bioprocesses. Challenges include scaling bacterial cultures, ensuring uniform particle size for reproducibility, and elucidating mechanistic pathways; future work should optimize bioreactor design for large-scale NP production and integrate these biogenic catalysts into membrane-electrode assemblies for performance validation [41].

Fe(III) Mimochrome VIa (FeMC6*a*), an artificial peroxidase "clicked" onto gold nanorods, nanoprisms and spheres to create bio-nanohybrid catalysts, chosen *for FeMC6*a's compact, robust oxidation scaffold and AuNMs' tunable plasmonics and high enzyme-loading capacity.

Although their study targets ABTS/H_2O_2 oxidation, the curved AuNM surfaces preserve native enzyme conformation, enhance interfacial electron transfer, and boost substrate adsorption; features readily repurposed for ORR by substituting O_2 as the electron acceptor. These bio-nanohybrids exhibit catalytic rates (k_{kat} ~$1–1.6 \times 10^2$ s^{-1}), Michaelis constants (K_m ~10^{-1}–10^2 mM) and stable performance under repeated cycles, all achieved via mild aqueous click chemistry. To translate this platform into practical fuel-cell catalysts, future work must replace ABTS/H_2O_2 assays with O_2 reduction tests, engineer efficient electrode immobilization and assess long-term durability under operating potentials [43]. Biomimetic, functionally graded composites of cellulose nanocrystals (CNCs), engineered proteins, and biomineralized apatite were engineered, drawing inspiration from the mantis shrimp's dactyl club. They leveraged plant-derived CNCs for their abundant, chiral-liquid-crystal assembly and proteins with liquid-liquid phase separation to template in situ CaP growth, producing stiff yet tough materials. Although not directly catalytic, the high-surface CNC framework and tunable porosity could act as supports for dispersed metal-oxide or non-precious metal NP catalysts, enabling enhanced adsorption and mass transport in fuel-cell electrodes. Should metal NPs be grafted onto these composites, electron pathways via the conductive protein/CNC network would facilitate charge transfer, and the hierarchical structure would offer abundant active sites. The all-biofabrication route minimizes reliance on toxic solvents, but adapting these composites for electrochemical use will demand conductive modifications, rigorous evaluation of electrical durability under potential cycling, and integration of catalytic sites without compromising mechanical integrity. [44].

Nacre-like films were created by genetically fusing resilin-like polypeptides with cellulose-binding modules and hydrophobin to assemble RGO and NFC layers in a brick-mortar fashion. Their pH-responsive linker allows fine control over interlayer spacing and ionic pathways, which for supercapacitors translates into low internal resistance and high capacitance. If repurposed as fuel-cell electrode scaffolds, the RGO/NFC network could host metal or metal-oxide NPs, where the protein bridges would ensure strong adhesion, rapid electron conduction, and efficient adsorption of reactants like O_2 or H_2. Although they do not report ORR/OER data, the films' conductivity (~680 $S \cdot cm^{-1}$) and mechanical resilience under bending indicate promising stability for cyclic electrochemical operation. This biosynthetic assembly method avoids harsh processing and could be scaled with recombinant protein production, but challenges include ensuring chemical compatibility with acidic or alkaline electrolytes and embedding sufficient catalytic loading without disrupting the responsive architecture [45]. Ultrathin BSA-templated sheets embedding 2–5 nm Pd nanoparticles (Pd_NP@BSAsheet) were produced via aqueous $PdCl_2$ reduction with L-ascorbic acid, exploiting BSA's tyrosine/histidine templating for controlled particle size and dispersion. The nanoscale Pd surfaces provide abundant H^+ adsorption sites and Michaelis–Menten-like kinetics in oxidase assays, suggesting strong intrinsic HER potential; the hybrid is thermally stable to 250 °C and recyclable over multiple cycles. The synthesis is green, low-Pd and economically promising, but actual HER metrics and integration into practical fuel-cell electrodes remain to be demonstrated. Key next steps are measuring HER activity on relevant support electrodes and proving electrode-level stability and mass transport [46]. Ultrathin (≈1.8 nm) phenylalanine–Cu^{2+} bio nanosheets formed by self-assembly and exfoliation, where phenylalanine drives chelation and covalent layered network formation and Cu^{2+}/Cu^{1+} redox sites enable fast electron transfer.

The nanosheets show redox kinetics ~10^5-fold faster than native laccase, stability across pH 3–9 and temperatures to 100 °C, and retain >80 % activity over 15 cycles, implying strong potential for HER after incorporation on conductive supports. Their minimal composition drastically reduces cost (~5,400× versus enzymes) and offers an ultra-minimalist, green catalyst platform. Remaining work must quantify HER rates and demonstrate electrode integration and long-term operational stability [47]. A soluble hydrogenase (SH)–based cofactor regeneration system for enzymatic cascades was developed. Mechanisms involve 100% atom-efficient NADH oxidation to NAD^+ with H_2 by-product and entropy-driven equilibrium shift upon H_2 removal. While no direct HER/ORR/OER metrics are provided, SH immobilized on electrodes could catalyze H_2 oxidation with low over potentials and clean by-product management. produces only clean H_2, operates without sparging, and avoids costly O_2 handling [48]. Engineered extremozymes (subtilisin, lipases, β-amylase, endoglucanase, lactonase, prolidase) via directed evolution, rational/semi-rational design, immobilization, solvent engineering, and in planta expression was surveyed. Extremozymes withstand harsh pH/temperature, reducing waste and extending operational windows. Mechanisms include enhanced active-site rigidity, optimized substrate binding, and reduced water solvation effects. Although no direct electrocatalytic data are reported, these robust enzymes, if deployed in fuel cells, could improve DET/MET kinetics, broaden pH/temperature tolerance, and resist electrochemical degradation. Engineered enzymes retain ≥80% activity after multiple cycles. Adapting extremozymes for electrode integration, scaling plant-based production, and engineering active sites for specific small-molecule electrocatalysis [49]. α-carboxysome protein shells that encapsulate an E. coli [NiFe] hydrogenase (HyaA/HyaB fused to a CsoS2-derived encapsulation peptide), expressing and self-assembling HyaAB Shell particles in E. coli BL21 (DE3) and purifying them by sucrose-gradient ultracentrifugation. The protein shell sterically excludes O_2 while admitting protons and HCO_3^-, the EP recruits and concentrates enzyme subunits to promote efficient electron transfer between Fe–S clusters and the Ni active site, and shell rigidity stabilizes enzyme conformation against heat and air.

Encapsulation boosts H_2 production 12–33× (in vitro and in vivo), preserves ≈88% activity after 24 h aerobic exposure versus ~13% for the free enzyme, and retains ~54% activity after 65 °C heat treatment compared with a ~33% decline for free HyaAB. Key challenges are scaling shell production with batch consistency, engineering permeability for external mediators or direct electrode wiring, and integrating these biocatalytic microreactors into electrode architectures for enzymatic fuel cells [50].

Table 6. Performance comparison: encapsulated HyaAB Shell versus free HyaAB EP.

Metric	Encapsulated Shell	Free HyaAB EP	Fold Increase
In vivo H_2 (anaerobic)	41,777.5 nmol L^{-1} h^{-1}	1,780.1	23×
In vivo H_2 (aerobic)	8,937.4 nmol L^{-1} h^{-1}	269.2	33×
In vitro H_2 (anaerobic rate)	543.4 nmol mg^{-1} min^{-1}	47.3	12×
O_2 Tolerance (24 h air)	Retains 88% activity	Retains 13%	—
Thermostability (65 °C, 20 min)	Retains 54% activity	33% decline	—

Bio-inspired materials such as self-healing polymers, microbial fuel cell mimics, bio-adhesives, water-harvesting surfaces, filtration matrices, and algae-derived biofuels were engineered by templating biological structures (salamander skin, mussel byssus, lotus leaf) onto polymer or ceramic scaffolds, embedding microcapsules for autonomous crack repair, and hybridizing silk fibroin or algae extracts with inorganic precursors to create hierarchical porosity and surface functionality. In a fuel-cell context these motifs would seal micro cracks to preserve electrode integrity, generate redox mediators to enhance electron transfer, use catechol-grafted adhesives to improve reactant adsorption, exploit lotus-leaf textures for three-phase water/gas management, and concentrate O_2 or H_2 at active sites via filtration motifs; electron transfer would proceed along biomimetic redox pathways while adsorption and kinetics follow functional-group affinities and enzyme-like Michaelis–Menten behaviour [51]. Non-precious nanozymes such as ferrihydrite, magnetosomes and biogenic Pd, Au and Ag nanoparticles produced by plants, bacteria and fungi in single-step, room-temperature aqueous routes using flavonoid- and protein-rich extracts, bacterial efflux precipitation or mycelial nucleation. These biogenic particles catalyze substrate oxidation at metal cores while biomolecular caps facilitate adsorption of H_2O_2 and organics and promote electron transfer from substrate to metal center using O_2 as acceptor, with kinetics often following Michaelis–Menten profiles tunable by particle size and capping chemistry. The water-based synthesis and biomolecule capping reduce cytotoxicity, enable use of agricultural by-products and support low-energy, low-waste production, while Pd and other biogenic NPs show superior kinetics versus chemically synthesized analogs. Remaining hurdles are scaling microbial or plant cultures to industrial volumes while keeping uniform particle morphology and activity, and future work should develop continuous-flow bioreactors, microbial engineering for tailored nanoparticle shapes, and embedding nanozymes into electrode matrices for direct ORR/HER evaluation [52].

Hybrid Catalysts

Hybrid composites represent a next-generation catalyst design strategy, combining distinct material classes to exploit synergistic effects. By integrating features such as enzyme-mimicking active centers within conductive carbon frameworks or embedding metal nanoparticles in porous supports, these catalysts unify high activity, selectivity, and durability. Such multifunctional architectures are particularly advantageous in fuel cell systems, where both efficient electron transport and stable active sites are essential for long-term performance.(Wu et al., 2020) developed Pt–Pd–3d-transition-metal ternary alloys (<50 at.% PGM) by wet-chemical synthesis (metal acetylacetonates in benzyl ether, oleylamine/oleic acid capping, reflux 220–260 °C) with NPs supported on Vulcan XC-72 and thermochemically treated (O_2/N_2 at 260 °C; H_2/N_2 at 400 °C) to induce lattice strain and remove organics. Thermochemical realloying and ADT-driven realloying regenerate a "stainless-like" alloy that resists dealloying, enabling significant PGM reduction while maintaining durability. For $Pt_{20}Pd_{20}Cu_{60}/C$ they report ECSA ≈ 60.7 m^2/g(Pt+Pd), MA = 1.66 A mg^{-1}_Pt (1.08 A mg^{-1}_Pt+Pd), with ~90% ECSA and 99.8% MA retained after 50k cycles; in-situ PEMFC testing sustained ~0.5 V at 0.23 A cm^{-2} for 70 h. DFT indicates Cu dissociation energies (0.33–0.52 eV), lowered OOH* activation (0.29 eV), and ~4.1% compressive strain that shift d-band centers to reduce ORR barriers; scale-up of wet syntheses, automotive cycling validation, exploration of PtPdNi/PtPdCo analogues, and MOF-templated supports are recommended [53].

Boron-doped palladium metallic nano-aerogels (Pd-MNAs) were developed to enhance the hydrogen oxidation reaction in alkaline media. Palladium's Pt-comparable HOR kinetics are tuned by sub-surface B-doping to optimize H*/OH* binding energies without surfactants or heavy Pt loadings. The synthesis employs surfactant-free wet chemistry: $NaBH_4$ reduction of Pd^{2+} at room temperature produces high-surface-area aerogels. Boron ingress is controlled by varying reductant-to-precursor (R:P) ratios (0.1:1, 1:1, 40:1) and injection speed/cooling (Pd-B40s, Pd-B40sc), achieving 0.47–11.5 at. % B. All steps occur in aqueous solution, require no post-annealing, and are scalable via simple mixing; DFT and EXAFS confirm octahedral sub-surface B incorporation rather than surface adsorption. Catalytic mechanisms revealed by DFT show B down-shifts the Pd d-band center—weakening H–Pd bonds to facilitate desorption and strengthening OH* adsorption, thereby balancing HOR kinetics; sub-surface B uniformly perturbs electronic structure and enhances electron transfer through the aerogel network, with optimal adsorption dynamics at ~ 2.7 at % B, accelerating the rate-limiting $H_2 \rightarrow 2H^* \rightarrow 2H^+ + 2e^-$ steps [59].

Table 7. Compact performance panorama of advanced Hybrid electrocatalysts.

Study (Year)	Key Features & Mechanism	Catalyst / Complex	Reaction	Voltages	Tafel slope (mV dec^{-1})	j & Mass activity	TOF (s^{-1})	Stability & Durability	Other parameters
[54]	Mo$_2$C nanoparticles (~10 nm) uniformly dispersed on biomass-derived N-doped carbon (kraft lignin); strong Mo$_2$C–NC interface promotes electron transfer; N defects adsorb protons and stabilize intermediates; Volmer–Heyrovsky pathway with electrochemical desorption RDS.	**Mo$_2$C/NC ; Commercial Mo$_2$C ; Unsupported Mo$_2$C ; Mo$_2$C/C**	HER	(η_{10} = **131 mV** @ 10 mA·cm^{-2} for **Mo$_2$C/NC** ; others not reported)	**58** (Mo$_2$C/NC); **97** (Commercial Mo$_2$C) ; **93** (Unsupported Mo$_2$C) ; **77** (Mo$_2$C/C)	-	-	**Mo$_2$C/NC:** retained activity over **3000 cycles** (η_{10} ↑15 mV); others: not reported	R_ct = **14.2 Ω** (Mo$_2$C/NC); Conductivity = **2.2×10^3 S·m^{-1}** (Mo$_2$C/NC), **1.1×10^2 S·m^{-1}** (Commercial Mo$_2$C), **6.5×10^2 S·m^{-1}** (Mo$_2$C/C); one-pot anneal @ **750 °C** from MoCl$_5$; gas-free synthesis; kraft lignin as C/N source.
[55]	Ligand-free Au$_{0.4}$Pt$_{0.6}$ nanoclusters grafted onto acid-treated CNT films; Pt(core)/AuPt(shell) lowers H adsorption; CNT network enhances electron transport; annealing removes ligands.	**Au$_{0.4}$Pt$_{0.6}$ NC on CNT film (AuPt NC CNT A)**	HER	(η = **27 mV** @ 10 mA·cm^{-2}; **89 mV** @ 100 mA·cm^{-2})	**57.3**	Mass activity = **7.49 A·mg^{-1}** (@100 mV); j @5 mA·cm^{-2}: not reported	**7.63** (@100 mV)	24 h durability at 10 mA·cm^{-2}: negligible overpotential drift	R_ct = **0.25 Ω**; DFT/XPS: Pt(core)/AuPt(shell); anneal 300 °C (N$_2$); low Pt loading via Au–Pt synergy.
[56]	Metal-free sp-N and B co-doped few-layer graphdiyne (sequential N→B doping): sp-N negative centers for H adsorption, B assists charge delocalization; water dissociation → H* recombination; conjugated channels for e$^-$ transfer.	**N,B-FLGDY-900 (few-layer graphdiyne)**	HER (alkaline)	(η_{10} = **84 mV** @ 10 mA·cm^{-2}; j = **48.6 mA·cm^{-2}** @ 0.25 V vs RHE)	**89**	j @5 mA·cm^{-2}: not reported; mass activity: not reported	not reported	**93%** current retention after **10,000 s** operation	Exfoliation/annealing sequence (grow on Cu → acid exfoliate → melamine N source → B$_2$O$_3$ anneal @ 900 °C); outperforms Pt/C stability (79%) in test.
[57]	Interpenetrating Ni$_2$P–NiSe$_2$ heterostructure aerogel from Ni hydrogel → freeze-dry → phosphidation/selenization; heterostructure charge flow tunes ΔG_H* ≈ 0 eV and moderates OH* adsorption for coupled HER + HMF oxidation.	**Ni$_2$P–NiSe$_2$ aerogel**	HER + 5-HMF oxidation (HMFOR)	(HER η_{10} = **68 mV** @ 10 mA·cm^{-2}; HMFOR onset = **1.30 V**)	**56**	j @5 mA·cm^{-2}: not reported; mass activity: not reported	not reported	**96%** current retention after **20 h** chrono	FDCA Faradaic efficiency = **97.4%**; two-electrode current boost **+102 mA·cm^{-2}** @ 1.50 V; EIS: R_ct significantly lower than single phase.
[58]	Transition-metal LDH nanosheets (NiFe, CoFe …): defect engineering, tunable interlayer spacing, hybridization with carbon supports; defect/edge sites facilitate OH*/O*/H* adsorption; heteroatom doping tunes d-band.	**LDH nanosheets (NiFe, CoFe)**	OER / HER / UOR (reviewed)	(OER η_{10} = **150–195 mV**; HER η_{10} = **12–63 mV**; UOR ≈ **1.3–1.4 V**)	OER: **30–60**; HER: **<50**; UOR: **~16**	j & mass activity: not reported (claims device-level parity with noble metals)	not reported	Stability: **thousands of cycles** in alkaline conditions reported	Synthesis: exfoliation & bottom-up growth; hybrid LDH@CNT improves transport; heteroatom doping (Ru, Ce, P).

Table 8. R:P ratios, boron content and relative HOR activity for Pd MNAs.

R:P Ratio	B Content (at. %)	Relative HOR Activity[1]
0.1:1	0.47	1.1× Pd
1:1	1.3	1.4× Pd
40:1	2.7	1.8× Pd (optimal)
40s*	6.7	1.5× Pd
40sc*	11.5	1.2× Pd

Table 9. Parameters and comparative alkaline-HER metrics for Mo_2C@BNC [60].

Metric / sample	Mo_2C@BNC	Mo_2C@NC	Mo_2C@C	Pt/C
η_{10} (mV @ 10 mA cm^{-2})	99	144	259	188
η_{100} (mV @ 100 mA cm^{-2})	168	—	—	188
Tafel slope (mV dec^{-1})	58.1	71.3	88.5	~30–40
Charge transfer Rct (Ω)	lowest	higher	highest	N/A
Stability (12 h @ 10 mA cm^{-2})	$\Delta\eta \approx + ?$	larger drift	larger drift	—

Relative to undoped Pd powder. Low B levels (2.7 at. %) yield maximal HOR currents; higher B reduces the active Pd surface and overall activity. While Tafel slopes and long-term cycling was not detailed—indicating a need for deeper durability studies—this strategy eliminates Pt use, lowers Pd requirements via ultra-dilute B doping, and employs ambient aqueous chemistry, minimizing energy and chemical waste. Future work must quantify and optimize durability under AEMFC cycling, validate full-cell integration and ionomer compatibility, explore bio-based reductants to replace $NaBH_4$, and extend impurity engineering to non-precious metal hosts (e.g., Ni, Fe) for broader green impact. Mo_2C@BNC, a B,N dual-doped carbon–encapsulated Mo_2C produced by one-pot pyrolysis of ammonium molybdate, dicyandiamide and boric acid, yielding ~3 nm Mo_2C cores wrapped in <3-layer doped carbon shells without harsh solvents. DFT and experiments show oxygen-deficient B sites accelerate H_2O dissociation (Volmer) while adjacent C sites tune H* binding for Heyrovsky/Tafel steps (ΔG_H_2O↓ and near-thermoneutral ΔG_H*), giving fast alkaline HER kinetics and the lowest Rct among comparisons. The carbon shell prevents corrosion and delivers ~12 h stability with minimal overpotential drift and the material shows much better η_{10} and η_{100} than Mo_2C@NC/@C. Translation to alkaline fuel-cell anodes is promising as Mo_2C@BNC could replace Pt in MEAs thanks to fast kinetics and low cost—provided membrane compatibility, ionomer–shell interfaces, thinner shells (<2 layers) for mass transport, biomass carbon sources, and long-term full-cell cycling (and spent-core recovery) are addressed [60].

A Mo_2C/graphene-nanowall (GNW) hybrid for HER was fabricated by ICP-CVD growth of GNWs on Papyex, Mo sputtering and carburizing anneal at 950 °C in Ar, with annealing time controlling Mo_2C particle size (10–20 nm); GNWs give very high surface area (~1100 m^2/g). The Mo_2C sites provide ΔG(H*) close to zero while GNWs supply fast electronic pathways; a 2–3 nm carbon shell protects Mo_2C from oxidation.

The Mo_2C/GNWs (4 min) sample gives η_{10} = 82 mV, Tafel slope 56 mV/dec, R_CT = 1.25 Ω, C_dl = 36.97 mF cm^{-2} and stable durability over 20 h, achieving Pt-comparable activity. Advantages include abundance of Mo/C and binder-free processing; challenges are lowering anneal temperature, controlling nanoparticle uniformity at scale and integrating into electrodes; future work should probe other carbides, GNW morphology tuning and bifunctional ORR coupling [61]. VO-Ru/HfO_2-OP, an oxygen-vacancy–rich, Ru-supported metal-oxide hybrid for alkaline HER was engineered, which may inform fuel-cell anode design. A polyol process with oleylamine/PVP yields ~ 60–80 nm HfO_2 particles decorated by 0.9 wt% Ru nanoparticles; subsequent H_2/Ar annealing introduces oxygen vacancies. Optimized Ru:Hf (1:1), PVP (50 mg), and oleylamine:PVP (4:50) ratios maximize Ru–O–Hf bond density and VO concentration. XANES/EXAFS confirm strong Ru–O–Hf interactions; DFT shows d-band tuning and reduced H_2O dissociation barriers (0.77→ 0.54 eV). This green, low-Ru strategy could inform self-humidifying anode layers in alkaline fuel cells by leveraging oxide supports for nanoparticle stabilization and water activation.

Table 10. Comparative alkaline-HER performance of VO Ru/HfO_2 OP, Ru/C and Pt/C.

Metric	**VO-Ru/HfO_2-OP**	**Ru/C**	**Pt/C**
η_{10} (mV)	39	79	~ 30
Mass Activity (@0.1 V, A mg_Ru^{-1})	20 × Pt/C	1 ×	1 ×
Tafel Slope (mV dec^{-1})	29	44	22
Rct (Ω)	49.1	higher	lower
Durability (5000 CV cycles)	+ 5 mV	+ 7 mV	N/A
Chrono (28 h @10 mA/cm^2)	stable	drift	—

Future directions include validating VO-Ru/HfO_2-OP in AEMFC assemblies, replacing oleylamine/PVP with bio-surfactants to reduce organic waste, scaling polyol routes via continuous flow reactors, and integrating catalyst recycling processes to recover Ru and HfO_2, thereby closing the material cycle [62]. N-doped porous carbon (N PC) / multi-walled CNT hybrids were prepared via CCVD on cobalt polymolybdate catalysts with MgO templating to produce a 4–86 nm pore distribution and high surface area. Nitrogen heteroatoms introduce adsorption/ active centers and enhanced charge transfer, while CNT networks provide conductive pathways for rapid electron transport, together improving catalytic kinetics and ion diffusion. Although ORR/HER values were not reported, the materials show strong energy-storage performance (148 F g^{-1} at 2 mV s^{-1}; 533 mAh g^{-1} after 10 cycles) and indicate good long-term structural/ electrochemical stability from templating and mechanical mixing. The authors highlight the metal-free catalyst potential for ORR and excellent conductivity but further electrocatalytic testing is needed [63]. Carbon-based CNT derivatives (CNT porins, assembled CNT architectures, CNT composites) and their fabrication routes were reviewed and CVD growth, self-insertion of CNT porins into lipid bilayers, Mn_3O_4 anchoring ("ear of wheat"), coaxial electrospinning of CNT/PDMS yarns, and layer-by-layer deposition (PANI/rGO/TA or PTCDA/NC) onto CNT scaffolds. They note CNTs' hollow nanochannels, tensile strength, high conductivity, and surface tunability enable rapid electron transfer, interlinked porosity for ion adsorption/diffusion, and surface groups that anchor catalytic sites and modulate ORR/OER selectivity; hydrophobic/ hydrophilic patterning also optimizes proton/gas flux. CNT systems can be produced by low-energy CVD or biomass pyrolysis, lower precious-metal loading and offer high durability; example performance includes Sn_4P_3@CNT/C as a sodium-ion anode (742 mAh g^{-1} capacity; 449 mAh g^{-1} rate). Main challenges are CNT bundling, large-scale alignment, and integrating biomass-derived CNTs with metal-oxide dopants; future directions include biomass-grown SWCNTs, in-situ electrochemical activation to raise active site density, and bifunctional CNT composites [64].

Non-precious Metals

Earth-abundant metals such as Fe, Co, and Ni have emerged as promising alternatives to precious metals in electrocatalysis due to their low cost, wide availability, and versatile redox chemistry. These non-precious metals can be engineered into various nanostructures or coordinated with heteroatoms to enhance catalytic activity and stability. Their unique electronic structures enable efficient catalysis in key energy conversion reactions such as the oxygen reduction, hydrogen evolution, and oxygen evolution reactions, making them attractive for sustainable fuel cell and electrolyzer technologies.

Group-10 metal chalcogenides ($PtSe_2$, $PtTe_2$, $PdTe_2$, $NiTe_2$ and mitrofanovite Pt_3Te_4) were investigated as lower-cost HER catalysts, growing single crystals by self-flux then exfoliating to ultrathin nanosheets or making bottom-up nanostructures to control morphology and defect density. Electronically these materials exploit Dirac-cone carriers for very fast electron transfer and use chalcogen vacancies to tune adsorption, giving Heyrovsky/Tafel-dominated kinetics and very low Tafel slopes (Pt_3Te_4 ≈ 32 mV·dec^{-1}; $NiTe_2$ nanotubes 59 mV·dec^{-1}; bulk $NiTe_2$ 183 mV·dec^{-1}). Pt_3Te_4 nanocrystals produce ultrahigh currents (>1000 mA·cm^{-2}), and surface-oxide passivation plus CO-inert surfaces improve stability in acid/alkali; Te substitution cuts raw material cost by ≈50% and synthesis is scalable. Remaining challenges are precise vacancy/defect control and sustainable Te recovery from industrial waste [65]. "Ni H_2–NH_3" (Ni nanoparticles on N-doped carbon from $Ni_3(BTC)_2$ MOF) was developed by pyrolysis at 390 °C in $H_2/NH_3/N_2$ to yield small Ni particles embedded in graphitized N-carbon, where NH_3 doping tunes the Ni d-band and H_2 prevents over-nitridation. D-band downshift (XPS/UPS) balances HBE/OHBE for fast HOR kinetics, KIE studies show OHBE limits the rate, and porous morphology improves mass transport; metrics: j_0,ECSA = 70 μA·cm_Ni^{-2}, mass current density @50 mV = 59.2 mA·mg_Ni^{-1}, PPD (PGM-free, 95 °C, H_2/O_2) = 488 mW·cm^{-2}, PPD (PGM-free, 80 °C) = 443 mW·cm^{-2}, PPD (with Pt/C cathode) = 628 mW·cm^{-2}, durability = 82% retention after 1,000

CV scans, long term 40 h @95 °C = 7% degradation. MOF precursors and benign pyrolysis gases support scalability and reduced footprint; future work should optimize NH_3 flow for dopant control and improve long-term cycling under real HEMFC loads [66]. (Y. Sun et al., 2020) prepared Fe–N doped carbon nanosheets (Fe N_3/C) by one-pot pyrolysis of glucose + $FeCl_3·6H_2O$ + dicyandiamide at 900 °C (acid leach), tuning N content (Fe N_1 → Fe N_3) and producing hierarchical meso/microporosity with BET ≈ 1,146 $m^2·g^{-1}$. The catalyst follows a dominant 4-electron ORR pathway via abundant pyridinic/pyrrolic N sites that lower O_2 adsorption energy, accelerating O_2 diffusion and charge transfer; performance: maximum power density = 912 $mW·m^{-2}$ (≈1.1× Pt/C), $E_1/_2$ shift = +14 mV vs Pt/C (−63 vs −77 mV), electron transfer number n ≈ 4.05, and kinetic current i_k at −0.45 V greater than Pt/C. The synthesis is straight forward and low-cost, but long-term continuous stability, batch reproducibility across biomass feedstocks and DFT mechanistic studies of Fe–N active sites remain priorities [67].

Transition-metal M–N–C single-atom and dual-atom catalysts were investigated and outlined mixing/pyrolysis and ZIF/MOF templating routes to anchor isolated Fe, Co, Mn atoms or pairs (FeCo, FeMn, MnCo) in N-doped carbon matrices. Reported performance: FeN_x/CoN_x single sites reach $E_1/_2$ ≈ 0.82–0.90 V and sustain ~10k cycles with <10 mV loss; MnN_x sites ≈ 0.815 V with 14 mV loss over 30k cycles; dual-atom catalysts (e.g., L-$CoFe_{0.5}$-NC) attain ≈145 $mW·cm^{-2}$ and $E_1/_2$ ≈ 0.77 V. These architectures approach near-100% atom utilization and strong intrinsic activity, but acid-phase stability still lags Pt/C and mechanistic clarity requires operando spectroscopy and DFT of dynamic active sites; scalability depends on MOF/biomass precursors and continuous pyrolysis, and lifecycle/circular-feedstock studies are needed to fully green hydrogen applications [68].

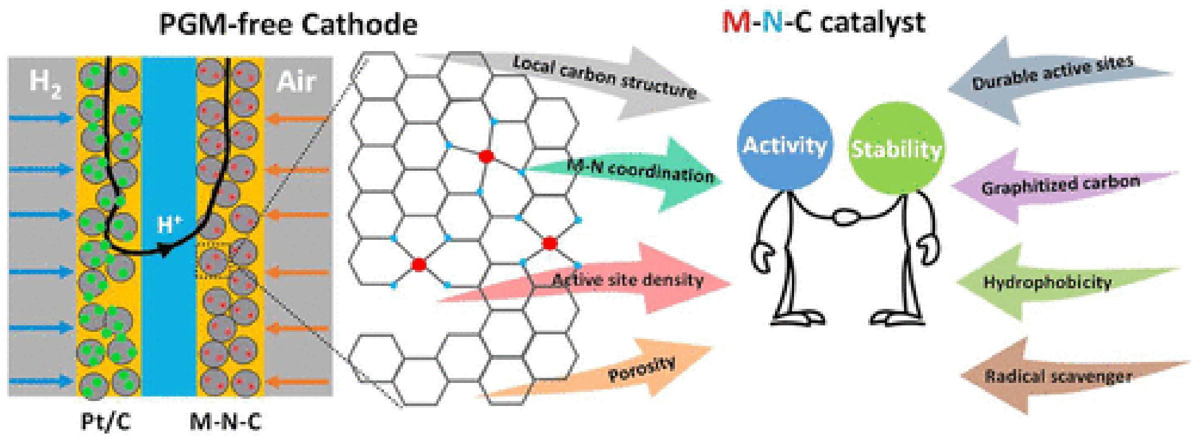

Figure 4. PGM-free cathode by utilizing M-N-C (Non-precious) metals materials.

Table 11. Key synthesis, mechanism and performance metrics for selected HER/ORR catalysts.

Study (Year)	Key features & mechanism	Catalyst	Reaction	Over-potential/ Onset	Tafel slope (mV dec^{-1})	j & Mass activity	TOF (s^{-1})	Other reported parameter
[69]	0.5 at% Fe doped b-Mo_2C in N-doped carbon; Fe/N synergy tunes Mo–H BE; porous C enhances transport; Volmer–Heyrovsky with Fe sites for H_2O dissociation	**Fe Mo_2C@NCF** (solid-state thermolysis, calcined 800 °C)	HER (acid, neutral, alkaline)	η_{10} = 65 mV (1 M KOH); 130 mV (1 M PBS); 129 mV (0.5 M H_2SO_4)	76 (KOH); 109 (PBS); 110 (H_2SO_4)	Exchange current density j_0 = 1.02 mA cm^{-2} (KOH)	—	Chrono 12 h: negligible degradation; 1000 CV cycles: minimal loss.
[70]	Atomically dispersed M–N_4 (Fe, Co) via sacrificial silica → mesoporous N-C; mixed-potential charge transfer (PRR 2e, ORR 4e at Fe-N-C)	**Fe N-C** (mesoporous N-C, Fe-N_4) ; **Co N-C** (mesoporous N-C, Co-N_4)	ORR & PRR (DBFC cathodes)	OCV: Fe N-C = 1.95 V ; Co N-C = 1.86 V. Mixed potential (Fe N-C)=0.87 V.	—	PPD: Fe N-C 0.209 W cm^{-2} ; Co N-C 0.144 W cm^{-2}.	—	Durability loss: Fe N-C 18.6 % ; Co N-C 6.7 %. Fe N-C higher mixed potential → higher OCV & power.

Study (Year)	Key features & mechanism	Catalyst	Reaction	Over-potential/ Onset	Tafel slope (mV dec^{-1})	j & Mass activity	TOF (s^{-1})	Other reported parameter
[71]	Single-atom M–N/C (M = Fe, Co, Ni, Mn, Sn, Sb, Bi) via ZIF-8 transmetalation; isolates metal vs N/C contributions; outer-sphere in alkali, inner-sphere on Fe/Co in acid	**Fe N/C** ; **Co N/C** ; **Fe/Co (mixed)** ; other M–N/C (Ni, Mn, Sn, Sb, Bi)	ORR (acid & alkaline)	—	~45 (Fe, Co in acid) ; (others not specified)	Activity vs N/C framework: Fe N/C 30× ; Co N/C 5× ; Fe/Co (alkali) 7×	—	H_2O_2 yield: Fe N/C 10–35 % ; Fe/Co (alkali) <25 %. Tafel slope SD = 4.8 mV dec^{-1}.
[72]	Co,Al,N tri-doped graphene (CANG); Co–N–C active sites bind H* (Volmer); Al tunes ΔG(H*)	**CANG (Co,Al,N tri-doped graphene)** ; **CNG (Co,N)** ; **ANG (Al,N)**	HER (acid)	η_{10}: CANG = 105 mV ; CNG = 180 mV ; ANG = 220 mV ; Pt/C=40 mV	81.5 (CANG) ; 120 (CNG) ; 150 (ANG) ; Pt/C ≈ 30	ECSA: CANG 48 m² g^{-1} ; CNG 30 ; ANG 25	CANG 0.3 s^{-1} ; CNG 0.1 s^{-1} ; ANG 0.05 s^{-1}	Stability: CANG minimal loss over 20,000 CV cycles. (Annealed 950 °C; acid leach.)
[73]	NiS_x layers electrodeposited on stainless-steel (SUS) meshes; sulfur tunes electron density to lower barrier	**NiS_x / SUS** (electrodeposited Ni → sulfurization → NiS_x 50–100 nm) ; **SUS (bare)**	HER (alkaline)	η_{10}: NiS_x/SUS = 258 mV ; SUS = 457 mV	100 (NiS_x/SUS) ; 170 (SUS)	ECSA improvement ≈ 100× (NiS_x/SUS vs SUS)	—	Stability: NiS_x/SUS sustained over 2000 cycles; bare SUS rapid decay. Challenges: stoichiometry control; detachment under bubble evolution.
[74]	Structurally precise M–N_4 SACs on CNTs (MPc/CNT & M-COF366/CNT); bridge O* adsorption lowers adsorption energies and scaling relations	**Ni-N_4 on CNT**; **Cu-N_4 on CNT** ; **Zn-N_4 on CNT** (structurally precise SACs)	ORR (acid & alkaline)	—	Tafel slope SD = 4.8 mV dec^{-1} (reported SD of slopes)	jk & onset: model–experiment excellent agreement across pH (no numeric jk provided)	TOF: Bridge O* model best matches experimental TOF (no numeric TOF provided	Stability concern: SAC aggregation under operating potentials; challenge to stabilize SACs for long-term operation.
[75]	Low-T hydrothermal CoOx–Fe_3O_4 on N-rGO; N anchors oxides to favor 4e ORR and suppress peroxide	**CoOx–Fe_3O_4 / N-rGO** (hydrothermal 150 °C)	ORR (AEMFC cathode)	Onset = 0.93 V vs RHE (@0.1 mA cm^{-2})	—	Limiting current: +12% vs Pt/C ; n ≈ 3.9 @ 0.80 V ; Peak power density (operando) = 676 mW cm^{-2} ; Mass activity = 2504 mW mg^{-1}	—	AST (5000 cycles): ~2 mV negative shift (vs 22 mV for Pt/C); voltage decay 5.6 mV h^{-1} (42 h).
[76]	Fe-doped cobalt hexacyanoferrate (PBA) films; mixed-valence Fe^{2+}–CN–Fe^{3+} for delocalized charge; binder-free aqueous films ≤150 °C	**$FeCo_2$ (parent PBA)** ; **$FeCo_{0.4}$ (optimum)**	Charge-transfer limited electrocatalysis / O–H activation	Onset overpotential ≈ 320 mV (both)	≈ 60 (both)	Current @ η=300 mV: $FeCo_2$ ≈ 50 mA cm^{-2} ; $FeCo_{0.4}$ > 100 mA cm^{-2} ; Max current: $FeCo_2$ ~80 ; $FeCo_{0.4}$ >150	—	Durability: 8 h neutral pH stable; acidic pH (<1.5) shows gradual decay. (Binder-free films; aqueous low-T route.)
[77]	Ultrafine nanoporous intermetallics (μ Co_7Mo_6, μ Fe_7Mo_6) by liquid-metal dealloying (~973 K); bicontinuous porosity, ~30 nm ligaments	**μ Co_7Mo_6 (powder)** ; **μ Co_7Mo_6 (self-supported sheet)**	HER	η_{10}: powder = 76 mV ; sheet ≈ near-zero onset	82 (powder) ; 46 (sheet)	(Sheet: near-Pt kinetics; no explicit mass activity provided)	—	Stability: sheets stable over 5k cycles and 48 h; powder shows near Pt kinetics. Challenges: brittleness, mass-transport limits.
[78]	Multinary CoMoFeNiCu HEAs designed to match Pt(111) HBE (–0.48 eV/H); ML-accelerated DFT screening; solid solution nanoparticles synthesized	**CoMoFeNiCu HEA compositions** (multiple screened & some synthesized; composition-specific data not detailed)	HER (design + experimental validation stage)	Descriptor: Pt(111) HBE = –0.48 eV/H ; predicted HEA HBE ≈ –0.48 eV/H	—	—	—	Predicted stability criteria: Ω > 1.1 ; lattice mismatch δr < 6.6% for majority compositions. Challenges: synthesize monodisperse HEAs, experimentally validate long-term HER stability.

Single-atom catalysts (SACs) on carbon and MOF-derived supports made by iced photochemical reduction were surveyed, MOF pyrolysis (UiO-66, ZIF-8 → atomically dispersed metals and dimers), CVD/ALD gas-phase deposition, pyrolysis of doped ZIF-8, and deliberate assembly of Fe–Co/Fe_2N_6 dimers—to maximize atom utilization and minimize PGM loading. Mechanistically, ORR at Pt–N and Fe–N sites follows a 4-electron pathway (elongated O–O ≈ 1.42 Å aids cleavage), $Pt–S_4$ sites favor 2-electron H_2O_2 generation, MOR on Pt SACs proceeds by direct O–H/C–H activation (high CO tolerance), FOR on Rh SACs follows a formate route, and non-PGM SACs (e.g., Mn) follow O → OOH → O + OH → H_2O sequences. Pt SACs operate at ultra-low loadings (0.09 $mg\cdot cm^{-2}$) delivering >680 $mW\cdot cm^{-2}$, Fe–N–C reaches ~360 $mW\cdot cm^{-2}$, and Mn SACs show only ~17 mV loss after 30,000 cycles; bimetallic dimers further enhance activity and durability while cutting noble-metal use by >90% and enabling earth-abundant, waste-derived supports. Remaining challenges: operando tracking of atom aggregation and support corrosion, scalable synthesis to ≥10 wt% loadings, rational multi-element dimer/trimer design for electronic tuning, and spatial confinement/support engineering to stabilise single atoms under fuel-cell conditions [79].

Table 12. Performance metrics.

Reaction	Catalyst	Key Metric	Stability
ORR	Pt_1@Fe N C	$E_{1/2}$ = 0.80 V; mass activity ×6.5 vs. NPs	12 mV $E_{1/2}$ loss after 10,000 cycles
ORR	Ir SAs	$E_{1/2}$ = 0.831 V; 6.44 W mgIr −1	—
ORR	Cu SAs/N C	$E_{1/2}$ = 0.895 V (vs. Pt/C 0.87 V)	—
MOR	Pt SACs	Activity ≥ 10× Pt/C; high CO tolerance	—
FOR	Rh SAs	16.1 A mg; 522.1 mW-1 mg	Stable over 50,000 s
ORR	Fe–Co dimer	0.98 W cm-2negligible voltage loss	Stable 100 h operation

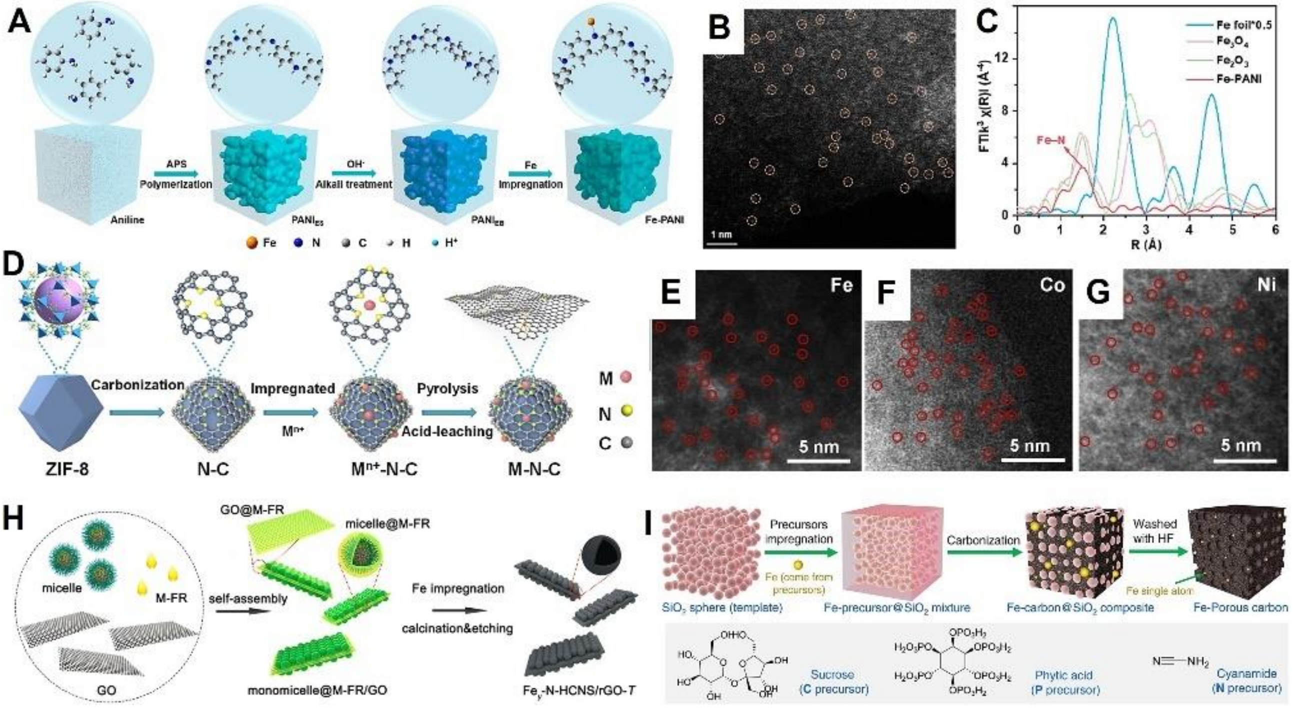

Figure 5. Example of Formation Preparation of Fe, Co, Ni-based non-precious catalysts [80].

Table 13. Key metrics for graphene-based HER catalysts.

Catalyst	η_{10} (mV)	Tafel (mV·dec^{-1})	Medium
NS 500	130	80.5	Acidic
Mo_2N–Mo_2C/HGr	18	68	Alkaline (>88 mA·cm^{-2})
NFO/rGO	5	59	Acidic
P WN/rGO	46	54	Acidic

Non-precious graphene-based HER catalysts were investigated (N,S-doped nanoporous graphene NS-500; holey rGO/Mo_2N–Mo_2C heterojunction Mo_2N–Mo_2C/HGr; NFO/rGO; and P-WN/rGO), synthesised from GO/rGO scaffolds by dopant insertion or embedding transition-metal compounds via co-precipitation, ball-milling and calcination, with Mo_2N and Mo_2C phases grown directly on holey rGO to yield a robust hybrid. Electronically, contiguous graphene networks give rapid electron transfer, dopant-induced defects and strong metal–carbon coupling create abundant H* adsorption sites and optimise H* adsorption/desorption kinetics. NS-500 exhibits good acidic HER activity while Mo_2N–Mo_2C/HGr outperforms Pt/C at high current densities; NFO/rGO's 5 mV overpotential and 59 mV·dec^{-1} Tafel slope reflect ultra-low barriers from strong electronic/chemical coupling, and P-WN/rGO achieves efficient acidic HER with enhanced charge distribution — all using earth-abundant elements and green fabrication that cut cost and environmental impact. Remaining challenges are scaling defect-controlled synthesis, ensuring long-term durability under cycling, and advancing hierarchical pore engineering, continuous-flow production and in-situ spectroscopy to optimise active-site density and mitigate carbon corrosion [81].

PGM-free M–N–C catalysts for PEMFC ORR were developed that span single-atom sites (Fe, Co, Mn, Cr) and dual-metal centers (Fe–Co, Fe–Mn, Fe–Zn), choosing transition metals because their unoccupied d-orbitals and lone pairs lower activation barriers while M–N–C frameworks provide high site dispersion. Their syntheses combine high-temperature pyrolysis of metal-phenanthroline–ZIF-8 precursors, heteroatom co-doping (O, P, S, B) to tailor electronic structure, surfactant-assisted MOF templating to maximise single-atom density, and NH_4Cl treatment to remove nanoparticles and yield atomically dispersed M–Nx sites. Mechanistically, electron transfer proceeds from metal centers into carbon shells, heteroatom dopants tune O_2 adsorption energies, and dual-metal synergy adjusts intermediate binding to accelerate four-electron ORR kinetics. Fe–N–C rivals Pt/C in acidic ORR, Co single-atom sites lower rate-determining barriers, Fe–Co binuclear centers boost activity and cycling stability, and Mn–N_4 matches Fe activity with superior durability; these materials leverage biomass-derived carbon and mild MOF routes to cut cost and pollution, while remaining challenges include acidic stability and precise multi-atom site engineering—future directions are DFT-guided site design, low-temperature pyrolysis, and hierarchical pore architectures [82].

Non-Pt ORR catalysts were reviewed including biomass-derived FeN_3S_1, Fe-, Cu-, Mn-, Zr-, Ru- and Ir-single atom sites, dual-atom and high-entropy alloys, and doped carbons for fuel cell applications. They emphasized low-cost, abundant alternatives to Pt/C that follow the four-electron pathway. Synthesis spans pyrolysis of metal–organic precursors, ball milling of heteroatom-doped carbons, fast-cooling dealloying for HEAs, sol-gel alloy formation, and MOF-derived templates. Mechanistically, SACs maximize metal utilization through unsaturated coordination environments, heteroatom doping tunes electronic structure and O_2 adsorption, and HEAs exploit "cocktail effects" to modulate binding energies and accelerate electron transfer [83].

Fe-SAs@NCTCs and O–Zr–N–C achieve ~0.9 V half-waves with outstanding stability, Ru-SSC matches Pt/C kinetics, and high-entropy alloys deliver durable $E_{1/2} = 0.90$ V. These green catalysts leverage biomass carbons and MOF routes to cut environmental impact. Challenges include industrial-scale synthesis of atomically precise sites and acidic-media activity gaps; future research will harness AI screening, low-energy templating, and recyclable feedstocks aligned with circular-economy principles.A Fe–N–S–C PGM-free cathode paired with a low-load Pt/C anode for PEMFCs, prepared by pyrolyzing Fe salt + S source + carbon precursor, formulating ink at 2.0 mg·cm^{-2} loading with Nafion (3:7 mass ratio), spraying onto Nafion-212 and hot-pressing the CCM/ GDL at 130 °C/ 500 psi in 2×2 cm^2 cells—fabrication avoids hazardous solvents and uses ≤150 °C process steps. Mechanistically, S/N dopants and high-surface-area carbon create abundant Fe–Nx active centers and graphitic domains for electron conduction, O_2 undergoes 4-electron reduction at Fe sites, the porous network retains water to mitigate membrane dehydration (self-humidification lowers charge transfer resistance at high current), and proton conduction occurs through Nafion channels intermingled with catalyst particles. Performance peaks at 283 mW·cm^{-2} (2.0 mg·cm^{-2}, 3:7 ionomer); RH effect was 217 → 246 mW·cm^{-2} (100% → 40% RH), back-pressure effect 142 → 223 mW·cm^{-2} (0 → 100 kPa), but durability shows a −40% cell-voltage drop after 30 h at 200 mA·cm^{-2}. The work halves Pt use and uses scalable spray/hot-press fabrication, yet key challenges are peroxide-induced carbon degradation (40% decay), developing peroxide decomposition additives or corrosion-resistant supports, controlling Fe–Nx speciation during pyrolysis, and implementing MEA-level recycling and Fe recovery [84]. PGM (Pt/C, PtRu/C) and PGM-free ($Fe_{0.5}$-950, Pd-CeO_2/C) catalysts combined with fluorine-free anion-exchange ionomers (FAA3, PPO-based) to enable greener AEMFCs by replacing toxic PEM chemistries were investigated. Catalytic inks, dispersing catalysts with Nafion, FAA3, or one of four PPO-AEIs at ionomer/catalyst ratios of 0.51 and 0.255 were prepared in bromide form, then exchanged in KOH during rotating disk electrode studies (0.1 M KOH). AEI films influence gas permeability, ion transport, and particle accessibility: PPO-AEIs form thinner, more permeable films than FAA3, enabling better O_2/H_2 diffusion; incomplete $Br^- \rightarrow OH^-$ exchange increases ionic resistance; insulating FAA3 films can electrically isolate low-density $Fe_{0.5}$-950 sites; cationic AEI groups adsorbing on PGM surfaces alter the double layer and HOR kinetics [85].

Table 14. Key Metric of electro-catalysts.

Catalyst	$E_1/_2$ (V)	Stability
Fe N_4/C	0.828	Comparable to Pt/C
CoSA–N–C	0.79	Comparable to Pt/C
FeCo–NC 3	0.842	11 mV drop / 10 k cycles
Mn–N_4	0.80	High, weak Fenton activity

Table 15. Electrocatalytic performance metrics of selected advanced catalysts compared to conventional Pt/C benchmarks.

Catalyst	$E_1/_2$ (V)	E_onset (V)	Durability
Fe-SAs@NCTCs	0.92	1.04	Exceeds Pt/C alternatives
O–Zr–N–C	0.91	N/A	Excellent (9.1 wt % loading)
Ru-SSC	0.824	0.92	18 mV shift/20 k cycles
Ordered HEA (OHEA)	0.90	N/A	0.01 V decay/10 k cycles

Table 16. Catalyst / AEI performance reproduced exactly from Santori et al. (2020) [85].

Catalyst / AEI	ORR Activity	HOR Activity	J_lim Variation	Bromide Retention
Pt/C + PPO-AEI	≈ Nafion	≈ Nafion	–	10–30 %
Pt/C + FAA3 (0.51)	Slight decrease	Severe suppression	–	10–30 %
Pt/C + FAA3 (0.255)	Baseline restored	Baseline restored	–	–
$Fe_{0.5}$-950 + FAA3	No activity	–	–	10–30 %
$Fe_{0.5}$-950 + PPO-AEIs	≈ Nafion w/↓J_lim	–	↓10–20 %	–
PtRu/C + PPO-AEIs	≈ Nafion	≈ Nafion	–	–
Pd-CeO_2/C + any AEI	–	< Nafion	–	–

Pt-based catalysts maintain near-baseline ORR/HOR with PPO-AEIs but suffer with FAA3 at high loading; PGM-free $Fe_{0.5}$-950 and Pd-CeO_2/C show greatly reduced activity with FAA3, only partially recovered at lower ionomer content; bromide retention of 10–30 % correlates with diminished diffusion-limited currents. Fluorine-free ionomers and PGM-lean catalysts reduce AEMFC cost and footprint, but AEIs with high OH^- conductivity and gas permeability are needed, along with protocols ensuring full counter-anion exchange. Future work should test full MEAs under operating AEMFC conditions and explore new polymer backbones balancing mechanical strength, ionic conductivity, and gas transport. Metal catalysts for biomass hydrogenation and HDO were investigated, favoring ultrasmall metals (Pt, Ru, Pd, Au, Ni, Co) and single-atom/cluster strategies to maximize metal utilization and suppress sintering/leaching; syntheses include PVP-capped Pt on mesoporous silica, soft-templated 3D Pt, $NaBH_4$ reduction for Pd, tannic-acid control for Ru clusters, calcination tuning for Au, organic-matrix deposition for high Ni dispersion and N-CNF anchoring for SACs. Mechanistically, activity is structure-sensitive (size-dependent H_2 and substrate adsorption), ligand/strain tune d-band positions, ensemble/bifunctional bimetallic effects enable sequential CO removal and hydrogenation, and SACs provide unique electronic states for elevated adsorption energies.

Ultrasmall Ru clusters give TOFs up to ~7× those of larger NPs; Pd SACs show 30–1,100× activity versus Pd NPs for succinic acid → GBL; Pd NPs (~2 nm) give ~100% CO_2 selectivity in formic acid dehydrogenation. Benefits are higher metal efficiency and reactivatability, while challenges include scalable, nuclearity-controlled SAC/cluster syntheses, direct SAC vs NP comparisons under fuel-cell conditions, and integration into continuous/membrane reactors, future directions emphasize biomass-derived hybrid supports and life-cycle analyses [86]. Ni-based catalysts (e.g., Ni/CeO_2, Ni–Cu/Al_2O_4) for H_2 production was evaluated, showing strong metal–support interactions enhance water dissociation and CO tolerance critical for fuel-cell electrodes; Ni sites catalyze O–H bond activation while Ni–Cu alloys tune electronic structure to improve H_2 and CO_2 selectivity. These low-cost, versatile catalysts leverage renewable feedstocks and promoter strategies to boost activity and selectivity, and their architectures can be adapted to improve ORR/MOR performance and long-term electrochemical stability. The study highlights economic and environmental benefits of Ni systems but notes the need to optimize support/ promoter combinations and to validate stability and selectivity in device-relevant cells [87]. Integral bulk electrodes of AlB_2-type transition-metal borides (TiB_2, ZrB_2, HfB_2) for PGM-free HER by high-pressure, high-temperature densification followed by targeted acid etching; compacted commercial TMB powders at **5 GPa and 1600 °C** and then etched in **12 M HCl** (TiB_2: 24 h; ZrB_2: 4 h; HfB_2: 2 h) to expose needle-, hump- or taper-like nanostructures. XPS confirmed core boride phases remain after etching while etching boosted surface area and active-site exposure; DFT indicates edge facets (e.g., $TiB_2(100)$) have lower H-adsorption free energy guiding selective facet exposure. The bulk, densified format gives low contact resistance and fast electron transport to adsorbed H* while the etched nanomorphologies shorten diffusion paths and accelerate Volmer–Heyrovsky kinetics, producing substantial performance gains (numerical metrics below in the Key Metric table). Replacing Pt with scalable HPHT + etching of abundant TMBs offers a cost-effective route, though the high HPHT energy input and integration into thin-film electrolyzers remain practical challenges; future work should explore lower-pressure densification, optimized etching protocols for scale, and full-cell electrolyzer testing for durability [88].

After densification and etching TiB_2 showed the largest overpotential reduction while ZrB_2 and HfB_2 also realized 40–44% improvements, and TiB_2 exhibited the lowest Tafel slope and charge resistance. The route replaces Pt with abundant borides and is promising for sustainable HER, but scaling must address HPHT energy costs and integration into thin-film electrolyzers. Surfactant-free Ta-based TaNOC nanospheres (mixed Ta_2O_5/Ta_4N_5/Ta_3N_5/TaN wrapped in carbon) produced by one-step laser pyrolysis of tantalum ethanolate with NH_3 vapour at grams-per-hour rates and isolated into TaNOC1–5; a 300 °C air post-anneal of TaNOC2 yields TaNOC2P with optimized surface area.

Table 17. HER performance of densified and etched AlB_2-type transition-metal borides.

Catalyst	Overpotential @10 mA cm^{-2}	Tafel Slope (mV dec^{-1})	Improvement vs. Powder
TiB_2 (HPHT)	477 mV	149.4	–
TiB_2 (HPHT + 24 h etch)	346 mV	–	61.9 %
ZrB_2 (HPHT + 4 h etch)	542 mV	–	40.3 %
HfB_2 (HPHT + 2 h etch)	515 mV	–	43.6 %

Electrochemically Ta_4N_5 is identified as the active redox site; TaNOC2P shows H_2O_2 reduction onset 0.51 V vs RHE (pH 7) with a relative current "3× TaNOC2" and 23 h steady operation, H_2O_2 reduction onset 0.62 V (pH 13) with "2× TaNOC2" and 23 h steady, H_2O_2 oxidation onset 1.10 V (pH 7) with 0.55 $mA \cdot cm^{-2}$ at 1.3 V and 23 h steady; full-cell tests sustained 8 h operation. Kinetic isotope effects confirm proton involvement at the RDS, the carbon shell supplies conductivity and gas access, partial oxides give structural stability, and the solvent-free laser route minimizes waste; tantalum is far cheaper than Pt. Remaining challenges are scaling laser pyrolysis beyond gram-scale, understanding long-term phase evolution and crossover in full cells, and integrating TaNOC into MEAs for peroxide-fuel or peroxide-carrier architectures [89]. Nitrogen-and-copper dual-doped molybdenum carbide (N–Cu–MoC) 2D nanosheets embedded in carbon from an organic–inorganic precursor (m-phenylenediamine + Cu salts + ammonium molybdate) followed by carburization, with CH_4/H_2 carburization used to produce undoped MoC controls—this systematic route yields single- and dual-doped analogs for direct performance comparison. Rationale and mechanism: dual N/Cu doping raise electron density at Mo sites and shifts the d-band to weaken Mo–H binding while 2D morphology and the conductive carbon matrix maximize edge/defect exposure and electron transfer; XPS shows increased Mo^{2+} fraction and Cu insertion causes lattice contraction that improves electrolyte access, and Tafel analysis indicates a Volmer–Heyrovsky pathway with an accelerated Heyrovsky step. Performance summary (qualitative): the dual-doped N–Cu–MoC sample outperforms MoC, N-MoC and Cu-MoC controls by showing the best overall kinetics, largest electrochemical active area and lowest charge-transfer resistance, and it demonstrates strong alkaline stability over extended cycling. Practical significance and next steps: the method uses inexpensive non-noble metals and scalable dual-doping chemistry, but future work must address full-cell durability, CO_2/impurity poisoning, MEA integration and testing in real alkaline electrolyze.

N–Cu–MoC attains the best combined metrics among the series (lowest overpotential and Tafel slope, highest exchange current and C_dl, and smallest R_ct) and shows durable operation in alkaline media; the synthesis avoids exotic salts and relies on inexpensive precursors. Remaining priorities are validating durability in full-cell MEAs, assessing impurity tolerance (CO_2, poisons), and scaling the dual-doping/carburization pathway for practical alkaline electrolyzer integration [90][91].

Table 18. HER performance of MoC derivatives (MoC, N-MoC, Cu-MoC, N-Cu-MoC) [90] [91].

Sample	η_{10} (mV)	Tafel Slope ($mV \cdot dec^{-1}$)	j_0 ($mA \cdot cm^{-2}$)	C_dl ($mF \cdot cm^{-2}$)	R_ct (Ω)	Stability
MoC	255	83.6	0.005	10.2	12	–
N MoC	227	–	–	–	–	–
Cu MoC	200	–	–	–	–	–
N Cu MoC	158	58	0.0185	26.1	3.3	30 h; >1000 cycles

Figure 6. Synthetic process of metal-organic framework nanosheet array [95].

Table 19. Representative metrics of MOFs.

Material (precursor → product)	ORR onset (V)	ORR n-electron	OER η_{10} (V)	HER η_{10}
ZIF-67 → Co@C	0.92	3.9	1.45	250 mV
Fe-MOF → Fe_3C@C	0.88	3.8	1.50	300 mV
Bimetal MOF → MNC	0.90	4.0	1.42	230

MOF Based Derivatives

Metal–Organic Frameworks (MOFs) and derivatives are crystalline, porous materials built from metal ions/clusters and organic linkers, offering exceptional surface areas and tunable pore architecture. They enable precise dispersion of catalytic metal sites and can be synthesized via greener routes (e.g. solvent-free or mechanochemical methods). Upon carbonization, MOF precursors produce N-doped carbon matrices with finely distributed transition metals, creating catalysts with tailored porosity and electronic structure for enhanced reaction kinetics. A hierarchical MOF-derived catalyst (BM Fe@NC T) made by solvent-minimal mechano chemical grinding of H_2BDC and $FeCl_3\cdot 6H_2O$ (120 min) and annealing at 800 °C for 3 h, followed by HCl leaching to produce Fe_3O_4/Fe_2C nanoparticles embedded in N-doped carbon. MOF templating gives uniform metal dispersion, tunable porosity and intimate Fe–C–N interfaces;

Fe_3O_4/Fe_2C dual sites and pyridinic/graphitic N jointly promote O_2 adsorption, 4-electron ORR ($n \approx 3.9$) and fast electron transfer via graphitized carbon. The catalyst matches Pt/C in half-wave potential and limiting current but shows higher Tafel slope (114 vs 89), superior durability ($\Delta E_{1/2} \approx -12$ mV after 3000 CV) and far better methanol tolerance (−3.8% vs −50% for Pt/C). The green, low-solvent route and high durability minimize footprint, though scale-up must preserve porosity and active site density and validate MEA/cell performance and circular recovery of carbon/Fe [92]. MOF/polymer hybrids by in-situ free-radical polymerization of MMA or DMAM inside Zr-MOFs (NU-1000, MOF-808) were created, producing uniformly dispersed polymer chains that improve mechanical adhesion, bridge MOF crystallites for electron transfer, and provide proton-conducting functional groups. The polymer networks preserve MOF porosity for small molecules and increase basicity (PDMAM), suggesting lower overpotentials and faster kinetics for ORR if tested in fuel-cell layers. Water-stability tests showed no MOF leaching after three soaks, indicating durable electrode layers in humid environments. The green, low-waste SALI/polymer steps are scalable for fiber coatings but require quantification of ORR/HER activities and long-term polymer stability under cyclic potentials [93]. A review survey of MOFs and MOF-derived carbons for energy electrodes, highlighting low-temperature, solvent-free syntheses (microwave, mechanochemical grinding) to tune porosity and produce high surface areas ideal for charge storage and catalysis.

Reported performance metrics for energy storage include 1345 mAh g^{-1} for H–Co–MOF and 251 F g^{-1} for Zn MOF-C, and long cycling stability (>5000 cycles for a carbonized MOF), implying MOF-derived carbons could withstand fuel-cell conditions. The authors note these frameworks' advantages permanent porosity, hierarchical pores and metal centers for improving electron transfer and reactant adsorption in fuel-cell catalysts. They call for direct ORR/OER testing and integration into gas-diffusion electrodes to bridge MOF materials into fuel-cell applications [94].

Aluminium, iron, zirconium and titanium-based MOFs were reviewed that immobilize metal nanoparticles for electrochemical sensing, emphasizing that MOFs' high surface area, tunable pores, Lewis-acidic nodes and thermal robustness lower overpotentials and improve charge transfer. They summarize diverse, scalable syntheses as hydrothermal and solvothermal crystallization, ultrasonic nanosheet formation, microwave-assisted morphology control, electrochemical deposition onto electrodes and mechanochemical grinding all aimed at increasing active-site exposure and enabling direct electrode integration. Mechanistically, metal nanoparticles confined within MOF pores amplify electrocatalytic currents by facilitating electron hopping while Lewis-acidic nodes enhance substrate adsorption and rapid redox cycling; overall kinetics therefore depend strongly on matching pore size to diffusive transport [96]. Review study on Al/Fe/Zr/Ti MOFs that immobilize metal nanoparticles for electrochemical sensing, stressing that MOFs' high surface area, tunable pores, Lewis-acid nodes and thermal robustness lower overpotentials and enhance charge transfer. They summarize diverse, scalable syntheses as hydrothermal/solvothermal crystallization, ultrasonic formation of nanosheets, microwave-assisted morphology control, electrochemical deposition onto electrodes and mechanochemical grinding each aimed at raising active-site exposure and enabling direct electrode integration. Mechanistically, metal nanoparticles confined in MOF pores amplify electrocatalytic currents by promoting electron hopping while Lewis-acidic nodes facilitate substrate adsorption and rapid redox cycling; overall kinetics depend strongly on matching pore size to diffusive transport. The review does not report ORR/OER/HER figures for fuel-cell reactions; reported strengths include good reusability but water-induced durability issues and conductor integration remain challenges [97]. MOF-based heterogeneous catalysis as a sustainable platform were discussed, where modular MOF topologies and tunable metal–linker chemistries allow embedding enzyme-like catalytic functions and sequential cascade transformations in a single solid matrix. The paper emphasizes engineered metal–linker microenvironments for precise electron transfer and selective substrate activation at Lewis-acidic nodes, but it does not detail specific synthetic protocols or quantitative electrocatalytic metrics. Although operational stability of MOF catalysts is noted, durability under harsh electrochemical conditions requires further development. Key future directions are scaling synthesis, preventing pore blockage and translating laboratory MOF architectures into industrial-scale fuel-cell electrodes, alongside hybrid materials and machine-learning guided design [98]. MOF-derived carbon nanocomposites as multifunctional electrocatalysts were reviewed, converting first-row transition-metal MOFs (Fe, Co, Ni, Mn) by pyrolysis into porous N-doped carbons that embed metal or metal-oxide nanoparticles. They explain that M–N_x active sites are effective for ORR, metal–oxide interfaces help OER, and heteroatom-doped carbon matrices support HER, while interconnected porosity enhances mass and electron transport and limits degradation. The review highlights strong bifunctional and trifunctional activity with minimal degradation, and it emphasizes one-pot pyrolysis scalability using earth-abundant metals; remaining challenges include sintering prevention, balancing porosity against conductivity and tailoring MOF precursors for multi-functionality. Representative performance numbers reported in the review are shown in the table below [99].

CONCLUSION

The collective evidence from the manuscript and attached data shows that green catalyst strategies that convert biomass wastes, exploit earth-abundant metals, mimic enzymatic active sites, and engineer MOF-derived single-atom sites provide a realistic pathway to reduce platinum-group metal dependence in hydrogen fuel-cell electrodes. Properly designed heteroatom-doped carbons and M–N_x motifs, especially when supported on hierarchically porous biomass-derived scaffolds, can achieve high metal utilization, favorable mass transport and ORR/HER metrics that approach platinum-class performance under alkaline conditions. Hybrid and bio-inspired platforms bring additional advantages of intrinsic selectivity and lower-toxicity synthesis routes, while MOF-derived single-atom catalysts uniquely enable atomically dispersed active centers with tunable coordination environments. However, three systemic gaps persist: reliable acidic-media performance and long-term stability under practical membrane-electrode-assembly operating conditions, scalable low-energy synthesis routes that avoid toxic reagents and minimize embodied energy, and cradle-to-grave material recovery, reuse and circularity validated by life-cycle assessment and techno-economic analysis. To bridge these gaps, research must prioritize device-level validation through standardized MEA testing, full-cell cycling and reporting at application-relevant current densities rather than relying solely on half-cell metrics. We also recommend integrating density functional theory and physics-aware machine-learning screening with targeted experimental kinetics to design atomically precise active sites that balance activity with intrinsic durability. Low-temperature, solvent-lean and mechanochemical or hydrothermal and plasma-assisted synthetic routes should be developed to reduce hazardous waste and scale-up risk. Operando and in-situ diagnostics such as X-ray absorption spectroscopy, Raman and FTIR spectroscopy, electrochemical mass spectrometry and transmission electron microscopy should be embedded within accelerated-stress protocols to map active-site evolution and identify dominant degradation pathways. Recycling-by-design must be adopted from the outset through recoverable supports, separable binders, magnetic or otherwise retrievable components, and closed-loop metal recovery workflows benchmarked by cradle-to-grave LCA and TEA. Attention to electrode engineering, including conductor integration, controlled pore connectivity and optimized ionomer distribution, will be essential to convert intrinsic material gains into practical power density and durability. Transparent benchmarking, open reporting of synthesis and testing protocols, and stronger industry–academia partnerships to de-risk pilot demonstrations will accelerate down-selection of promising candidates. If these coordinated scientific, engineering and lifecycle priorities are pursued, green catalyst platforms can move from academic promise to commercial reality, enabling low-cost, low-carbon and circular hydrogen fuel-cell technologies.

ACKNOWLEDGEMENTS

The authors express their gratitude to the Ministry of Higher Education (MoHE) for the generous financial support provided under the Long-Term Research Grant Scheme (SATREPS 2023: 1.2) with grant vote number R.J130000.7809.4L976 (SATREPS 2023: 1.2). This study was also supported by the Science and Technology Research Partnership for Sustainable Development (SATREPS), which is a collaborative effort between the Japan Science and Technology Agency (JST) and the Japan International Cooperation Agency (JICA).

AUTHORS' CONTRIBUTIONS

Zargham S. Cheema: conceptualization, literature collection, and synthesis, drafting of the manuscript, preparation of figures and tables.

Juhana Jaafar: supervision, critical revision of intellectual content, editing and final approval of the manuscript.

Both authors discussed the structure and scope of the review, contributed to interpretation of the literature, and agree to be accountable for all aspects of the work.

CONFLICTS OF INTEREST

The authors declare that they have no known competing financial interests or personal relationships that could have appeared to influence the work reported in this paper.

ORCID (if any)
Juhana Jaafar[1,*] https://orcid.org/0000-0002-7245-8155

REFERENCES

1. Shetty, A., Molahalli, V., Sharma, A. and Hegde, G. (2023) Biomass-derived carbon materials in heterogeneous catalysis: A step towards sustainable future. *Catalysts*, **13(1)**.

2. Ding, Y., Greiner, M., Schlögl, R. and Heumann, S. (2020) A metal-free electrode: From biomass-derived carbon to hydrogen. *ChemSusChem*, **13(16)**, 4064–4068.

3. Guchhait, S. K., Khatana, S., Saini, R. K., Pranay, Singh, A. D. and Sarma, A. K. (2024) Recent advances in biomass derived nano-structured carbon materials for low-temperature fuel cell application. *Applied Catalysis O: Open*, **189**, 206924.

4. Mugadza, K., Stark, A., Ndungu, P. G. and Nyamori, V. O. (2020) Synthesis of carbon nanomaterials from biomass utilizing ionic liquids for potential application in solar energy conversion and storage. *Materials,* **13(18)**.

5. Li, Z., Feng, Y., Qu, X., Yang, Y., Dong, L., Lei, T. and Ren, S. (2023) Impact of different lignin sources on nitrogen-doped porous carbon toward the electrocatalytic oxygen reduction reaction. *International Journal of Environmental Research and Public Health*, **20(5)**.

6. Schonvogel, D., Nowotny, M., Woriescheck, T., Multhaupt, H., Wagner, P., Dyck, A., Agert, C. and Wark, M. (2019) Hydrothermal carbonization-derived carbon from waste biomass as renewable Pt support for fuel cell applications: Role of carbon activation. *Energy Technology*, **7(11)**.

7. Guo, C., Sun, L., Liao, W. and Li, Z. (2016) The use of an edible mushroom-derived renewable carbon material as a highly stable electrocatalyst towards four-electron oxygen reduction. *Materials*, **9(1)**.

8. Jung, H., Kang, J., Nam, I. and Bae, S. (2020) Graphitic porous carbon derived from waste coffee sludge for energy storage. *Materials*, **13(18)**.

9. Perumal, S., Kishore, S. C., Atchudan, R., Sundramoorthy, A. K., Alagan, M. and Lee, Y. R. (2022) Sustainable synthesis of N/S-doped porous carbon from waste-biomass as electroactive material for energy harvesting. *Catalysts*, **12(4)**.

10. Testa, D., Zuccante, G., Muhyuddin, M., Landone, R., Scommegna, A., Lorenzi, R., Acciarri, M., Petri, E., Soavi, F., Poggini, L., Capozzoli, L., Lavacchi, A., Lamanna, N., Franzetti, A., Zoia, L. and Santoro, C. (2023) Giving new life to waste cigarette butts: Transformation into platinum group metal-free electrocatalysts for oxygen reduction reaction in acid, neutral and alkaline environment. *Catalysts*, **13(3)**.

11. Barrio, J., Pedersen, A., Favero, S., Luo, H., Wang, M., Sarma, S. C., Feng, J., Ngoc, L. T. T., Kellner, S., Li, A. Y., Jorge Sobrido, A. B. and Titirici, M. M. (2023) Bioinspired and bioderived aqueous electrocatalysis. *Chemical Reviews*, **123(5)**, 2311–2348.

12. Breitenbach, S., Gavrilov, N., Pašti, I., Unterweger, C., Duchoslav, J., Stifter, D., Hassel, A. W. and Fürst, C. (2021) Biomass-derived carbons as versatile materials for energy-related applications: Capacitive properties vs. oxygen reduction reaction catalysis. *Catalysts*, **7(3)**, 55.

13. Islam, Md. T., Howlader, Md. S., Shuvo, D. M. and Kamal Uddin, Md. (2023) Carbon fiber from biomass sources: A comprehensive review. *Non-Metallic Material Science*, **5(1)**, 14–26.

14. Giannakoudakis, D. A., Zormpa, F. F., Margellou, A. G., Qayyum, A., Colmenares-Quintero, R. F., Len, C., Colmenares, J. C. and Triantafyllidis, K. S. (2022) Carbon-based nanocatalysts (CnCs) for biomass valorization and hazardous organics remediation. *Nanomaterials*, **12(10)**.

15. Pagett, M., Teng, K. S., Sullivan, G. and Zhang, W. (2023) Reusing waste coffee grounds as electrode materials: Recent advances and future opportunities. *Global Challenges*, **7(1)**.

16. Biemolt, J., Rothenberg, G. and Yan, N. (2019) Understanding the roles of amorphous domains and oxygen-containing groups of nitrogen-doped carbon in oxygen reduction catalysis: Toward superior activity. *Inorganic Chemistry Frontiers*, **7(1)**, 177–185.

17. Magagula, L. P., Masemola, C. M., Ballim, M. A., Tetana, Z. N., Moloto, N. and Linganiso, E. C. (2022) Lignocellulosic biomass waste-derived cellulose nanocrystals and carbon nanomaterials: A review. *International Journal of Molecular Sciences*, **23(8)**.

18. Destyorini, F., Irmawati, Y., Hardiansyah, A., Widodo, H., Yahya, I. N. D., Indayaningsih, N., Yudianti, R., Hsu, Y. I. and Uyama, H. (2021) Formation of nanostructured graphitic carbon from coconut waste via low-temperature catalytic graphitisation. *Engineering Science and Technology, an International Journal*, **24(2)**, 514–523.

19. Wang, K., Cao, Y., Wang, X., Kharel, P. R., Gibbons, W., Luo, B., Gu, Z., Fan, Q. and Metzger, L. (2016) Nickel catalytic graphitized porous carbon as electrode material for high performance supercapacitors. *Energy*, **101**, 9–15.

20. Sun, Z., Yao, D., Cao, C., Zhang, Z., Zhang, L., Zhu, H., Yuan, Q. and Yi, B. (2022) Preparation and formation mechanism of biomass-based graphite carbon catalyzed by iron nitrate under a low-temperature condition. *Journal of Environmental Management*, **318**.

21. Li, J., Zhang, Z., Wang, Z., Cao, Q., Guo, F. and Cao, Q. (2022) Low temperature graphitization and electrochemical properties of porous carbon catalyzed with bimetal Ni-Mo. *Diamond and Related Materials*, **123**.

22. Tan, Y., Xu, Z., He, L. and Li, H. (2022) Three-dimensional high graphitic porous biomass carbon from dandelion flower activated by K2FeO4 for supercapacitor electrode. *Journal of Energy Storage*, **52**.

23. Zha, Z., Zhang, Z., Xiang, P., Zhu, H., Shi, X. and Chen, S. (2021) Porous graphitic carbon from mangosteen peel as efficient electrocatalyst in microbial fuel cells. *Science of the Total Environment*, **764**.

24. Major, I., Pin, J. M., Behazin, E., Rodriguez-Uribe, A., Misra, M. and Mohanty, A. (2018) Graphitization of Miscanthus grass biocarbon enhanced by in situ generated FeCo nanoparticles. *Green Chemistry*, **20(10)**, 2269–2278.

25. Jabarullah, N. H., Kamal, A. S. and Othman, R. (2021) A modification of palm waste lignocellulosic materials into biographite using iron and nickel catalyst. *Processes*, **9(6)**.

26. Sekar, S., Sim, D. H. and Lee, S. (2022) Excellent Electrocatalytic Hydrogen Evolution Reaction Performances of Partially Graphitized Activated-Carbon Nanobundles Derived from Biomass Human Hair Wastes. *Nanomaterials*, **12(3)**.

27. John, K. I. and Omorogie, M. O. (2022) Biomass-based hydrothermal carbons for catalysis and environmental cleanup: a review. *Green Chemistry Letters and Reviews*, **15(1)**, 160–184.

28. Predeanu, G., Slăvescu, V., Drăgoescu, M. F., Bălănescu, N. M., Fiti, A., Meghea, A., Samoila, P., Harabagiu, V., Ignat, M., Manea-Saghin, A. M., Vasile, B. S. and Badea, N. (2023) Green Synthesis of Advanced Carbon Materials Used as Precursors for Adsorbents Applied in Wastewater Treatment. *Materials*, **16(3)**.

29. Bhattacharyya, P., Parmar, P. R., Basak, S., Dubey, K. K., Sutradhar, S., Bandyopadhyay, D. and Chakrabarti, S. (2023) Metal organic framework-derived recyclable magnetic coral Co@Co3O4/C for adsorptive removal of antibiotics from wastewater. *Environmental Science and Pollution Research*, **30(17)**, 50520–50536.

30. Tseng, F. G., Bhalothia, D., Lo, K. H., Syu, C. H., Chen, Y. C., Sihag, A., Wang, C. W., Chen, H. Y. T. and Chen, T. Y. (2024) Glucose-based highly-porous activated carbon nanospheres (g-ACNSs) for high capacity hydrogen storage. *Energy Advances*, **3(6)**, 1283–1292.

31. Seo, M. J. and Schmidt-Dannert, C. (2021) Organizing multi-enzyme systems into programmable materials for biocatalysis. *Catalysts*, **11(4)**.

32. Nguyen, D. N., Sim, U. and Kim, J. K. (2020) Biopolymer-inspired N-doped nanocarbon using carbonized polydopamine: A high-performance electrocatalyst for hydrogen-evolution reaction. *Polymers*, **12(4)**.

33. Cebollada, J., Sebastián, D., Lázaro, M. J. and Martínez-Huerta, M. V. (2023) Carbonized Polydopamine-Based Nanocomposites: The Effect of Transition Metals on the Oxygen Electro-catalytic Activity. *Nanomaterials*, **13(9)**.

34. Schild, J., Reuillard, B., Morozan, A., Chenevier, P., Gravel, E., Doris, E. and Artero, V. (2021) Approaching industrially relevant current densities for hydrogen oxidation with a bioinspired

molecular catalytic material. *Journal of the American Chemical Society*, **143**, 18150–18158.

35. Hirai, Y., Ishibashi, K., Oku, K., Ito, K. and Yabu, H. (2024) Rare-metal-free hydrogen evolution reaction electrocatalysts based on metal azaphthalocyanine molecular layer for anion exchange membrane water electrolysis. *Discover Chemical Engineering*, **4(1)**.

36. Kiciński, W. and Dyjak, S. (2021) Nitrogen-doped carbons derived from imidazole-based cross-linked porous organic polymers. *Molecules*, **26(3)**.

37. Wang, Q., Chen, K., Jiang, H., Chen, C., Xiong, C., Chen, M., Xu, J., Gao, X., Xu, S., Zhou, H. and Wu, Y. (2023) Cell-inspired design of cascade catalysis system by 3D spatially separated active sites. *Nature Communications*, **14(1)**.

38. Milton, R. D. (2024) Electron-Transferring Metalloenzymes and their Potential Biotechnological Applications. *Chimia*, **78(1–2)**, 13.

39. Leone, L., Sgueglia, G., La Gatta, S., Chino, M., Nastri, F. and Lombardi, A. (2023) Enzymatic and Bioinspired Systems for Hydrogen Production. *International Journal of Molecular Sciences*, **24(10)**.

40. Valetti, F., Morra, S., Barbieri, L., Dezzani, S., Ratto, A., Catucci, G., Sadeghi, S. J. and Gilardi, G. (2024) Oxygen-resistant [FeFe]hydrogenases: new biocatalysis tools for clean energy and cascade reactions. *Faraday Discussions*, **252**, 223–240.

41. Tsekhmistrenko, S. I., Bityutskyy, V. S., Tsekhmistrenko, O. S., Horalskyi, L. P., Tymoshok, N. O. and Spivak, M. Y. (2020) Bacterial synthesis of nanoparticles: A green approach. *Biosystems Diversity*, **28(1)**, 9–17.

42. Barrio, J., Pedersen, A., Favero, S., Luo, H., Wang, M., Sarma, S. C., Feng, J., Ngoc, L. T. T., Kellner, S., Li, A. Y., Jorge Sobrido, A. B. and Titirici, M. M. (2023) Bioinspired and Bioderived Aqueous Electrocatalysis. *Chemical Reviews*, **123(5)**, 2311–2348.

43. Renzi, E., Esposito, A., Leone, L., Chávez, M., Pineda, T., Lombardi, A. and Nastri, F. (2024) Biohybrid materials comprising an artificial peroxidase and differently shaped gold nanoparticles. *Nanoscale Advances*, **6(14)**, 3533–35442.

44. Mohammadi, P., Gandier, J. -A., Nonappa, N., Wagermaier, W., Miserez, A. and Penttilä, M. (2021) Bioinspired functionally graded composite assembled using cellulose nanocrystals and genetically engineered proteins with controlled biomineralization. *Preprint*.

45. Dhar, P., Phiri, J., Szilvay, G. R., Westerholm-Parvinen, A., Maloney, T. and Laaksonen, P. (2020) Genetically engineered protein based nacre-like nanocomposites with superior mechanical and electrochemical performance. *Journal of Materials Chemistry A*, **8(2)**, 656–669.

46. Polepalli, S., Uttam, B. and Rao, C. P. (2020) Protein-inorganic nano hybrid sheets of Pd embedded BSA as a robust catalyst in water for oxidase mimic activity and C–C coupling reactions, and as a sustainable material for micromolar sensing of dopamine. *Materials Advances*, **1(6)**, 2074–2083.

47. Makam, P., Yamijala, S. S. R. K. C., Bhadram, V. S., Shimon, L. J. W., Wong, B. M. and Gazit, E. (2022) Single amino acid bionanozyme for environmental remediation. *Nature Communications*, **13(1)**.

48. Al-Shameri, A., Siebert, D. L., Sutiono, S., Lauterbach, L. and Sieber, V. (2023) Hydrogenase-based oxidative biocatalysis without oxygen. *Nature Communications*, **14(1)**.

49. Chatterjee, A., Puri, S., Sharma, P. K., Deepa, P. R. and Chowdhury, S. (2023) Nature-inspired Enzyme engineering and sustainable catalysis: biochemical clues from the world of plants and extremophiles. *Frontiers in Bioengineering and Biotechnology*, **11**.

50. Jiang, Q., Li, T., Yang, J., Aitchison, C. M., Huang, J., Chen, Y., Huang, F., Wang, Q., Cooper, A. I. and Liu, L. N. (2023) Synthetic engineering of a new biocatalyst encapsulating [NiFe]-hydrogenases for enhanced hydrogen production. *Journal of Materials Chemistry B*, **11(12)**, 2684–2692.

51. Barman, A. and Das, K. (2024) Bio-Inspired Products and Technology Innovation– The Present and Future. *International Journal of Innovative Research in Engineering and Management*, **11(3)**, 25–33.

52. Ngcongco, K., Krishna, S. B. N. and Pillay, K. (2023) Biogenic metallic nanoparticles as enzyme mimicking agents. *Frontiers in Chemistry*, **11**.

53. Wu, Z., Maswadeh, Y., Wen, J., Kong, Z., Shan, S., Vargas, J., Yan, S., Hopkins, E., Park, K., Sharma, A., Ren, Y., Petkov, V., Wang, L. and Zhong, C. -J. (2020) Alloying–Realloying Enabled High Durability for Pt–Pd–3d-Transition Metal Nanoparticle Fuel Cell Catalysts. *Preprint*.

54. Oh, N. Y., Lee, G. H., Jeong, H. M., Kim, Y. S. and Youn, D. H. (2021) Kraft Lignin Derived Molybdenum Carbide/Nitrogen-Doped Carbon Composite for Efficient Hydrogen Evolution Reaction. *Journal of The Electrochemical Society*, **168(8)**, 084511.

55. Kang, J., Kloppenburg, J., Sheng, J., Xu, Z., Meinander, K., Jiang, H., Lv, Z. -P., Kauppinen, E. I., Zhang, Q., Chen, X., Ikkala, O., Caro, M. A. and Peng, B. (2024) Anomalous Enhancement of the Electrocatalytic Hydrogen Evolution Reaction in AuPt Nanoclusters. arXiv:2406.08580.

56. Zhao, Y., Yang, N., Wang, C., Song, L., Yu, R. and Wang, D. (2021) Boosting hydrogen evolution reaction on few-layer graphdiyne by sp-N and B co-doping. *APL Materials*, **9(7)**.

57. Liu, H., Yang, F., Chen, Z., Qian, J., Wang, J., Wu, N. and Li, Y. (n.d.) Transition-Metal-Selenides Based Aerogel for Highly Efficient Electrocatalytic Hydrogen Evolution and 5-hydroxymethylfurfural Oxidation.

58. Wang, Y., Zhang, M., Liu, Y., Zheng, Z., Liu, B., Chen, M., Guan, G., Yan, K., et al. (2017) Recent Advances on Transition-Metal-Based Layered Double Hydroxides Nanosheets for Electrocatalytic Energy Conversion

59. Kim, S. -H., Yoo, S. -H., Shin, S., El-Zoka, A. A., Kasian, O., Lim, J., Jeong, J., Scheu, C., Neugebauer, J., Lee, H., Todorova, M. and Gault, B. (n.d.) Controlled doping of electrocatalysts through engineering impurities.

60. Zhou, M., Jiang, X., Kong, W., Li, H., Lu, F., Zhou, X. and Zhang, Y. (2023) Synergistic Effect of Dual-Doped Carbon on Mo2C Nanocrystals Facilitates Alkaline Hydrogen Evolution. *Nano-Micro Letters*, **15(1)**.

61. Chaitoglou, S., Amade, R., Ospina, R. and Bertran-Serra, E. (2023) Hybrid Nanostructured Compounds of Mo2C on Vertical Graphene Nanoflakes for a Highly Efficient Hydrogen Evolution Reaction. *ACS Applied Energy Materials*, **6(11)**, 6120–6131.

62. Li, G., Jang, H., Liu, S., Li, Z., Kim, M. G., Qin, Q., Liu, X. and Cho, J. (2022) The synergistic effect of Hf-O-Ru bonds and oxygen vacancies in Ru/HfO2 for enhanced hydrogen evolution. *Nature Communications*, **13(1)**.

63. Malozyomov, B. V., Kukartsev, V. V., Martyushev, N. V., Kondratiev, V. V., Klyuev, R. V. and Karlina, A. I. (2023) Improvement of Hybrid Electrode Material Synthesis for Energy Accumulators Based on Carbon Nanotubes and Porous Structures. *Micromachines*, **14(7)**.

64. Fan, Y., Hou, Y., Wang, M., Zheng, J. and Hou, X. (2022) Bioinspired carbon nanotube-based materials. *Materials Advances*, **3(7)**, 3070–3088.

65. D'Olimpio, G., Santoro, S., Kuo, C. N., Ottaviano, L., Lue, C. S., Boukhvalov, D. W. and Politano, A. (2022) Sustainable Hydrogen Production Using Group-10 Metal Chalcogenides as Low-Cost Effective Electrocatalysts. *Advanced Sustainable Systems*, **6(10)**.

66. Ni, W., Wang, T., Héroguel, F., Krammer, A., Lee, S., Yao, L., Schüler, A., Luterbacher, J. S., Yan, Y. and Hu, X. (2022) An efficient nickel hydrogen oxidation catalyst for hydroxide exchange membrane fuel cells. *Nature Materials*, **21(7)**, 804–810.

67. Sun, Y., Zhang, Z. Z., Sun, Y. M. and Yang, G. X. (2020) One-pot pyrolysis route to Fe−N-doped carbon nanosheets with outstanding electrochemical performance as cathode materials for microbial fuel cell. *International Journal of Agricultural and Biological Engineering*, **13(6)**, 207–214.

68. Hao, Z., Ma, Y., Chen, Y., Fu, P. and Wang, P. (2022) Non-Noble Metal Catalysts in Cathodic Oxygen Reduction Reaction of Proton Exchange Membrane Fuel Cells: Recent Advances. *Nanomaterials*, **12(19)**.

69. Huang, J., Wang, J., Xie, R., Tian, Z., Chai, G., Zhang, Y., Lai, F., He, G., Liu, C., Liu, T., Shearing, P. R. and Brett, D. J. L. (2020) A universal pH range and a highly efficient Mo2C-based electrocatalyst for the hydrogen evolution reaction. *Journal of Materials Chemistry A*, **8(38)**, 19879–19886.

70. Ko, Y., Park, J., Zhang, X., Kang, L., Ha, T., Pham, M., Boureau, V., Pham-Huu, C., Kim, J., Zhong, L. and Züttel, A. (n.d.) Durable M-N-C Catalysts for Oxygen Reduction Reaction (ORR) and Hydrogen Peroxide Reduction Reaction (PRR) in Platinum Group Metal-Free Direct Borohydride Fuel Cells.

71. Gong, M., Mehmood, A., Ali, B., Nam, K. W. and Kucernak, A. (2023) Oxygen Reduction Reaction Activity in Non-Precious Single-Atom (M-N/C) Catalysts─Contribution of Metal and Carbon/Nitrogen Framework-Based Sites. *ACS Catalysis*, **13(10)**, 6661–6674.

72. Zhou, X., Yu, H., Liu, Y., Kong, Y., Tao, Y. and Qin, Y. (2019) Boosting the hydrogen evolution

activity of a Co-N-C electrocatalyst by codoping with Al. *RSC Advances*, **9(58)**, 33997–34003.

73. TD, D. (2023) Nano-Nickel as a Catalyst for the Ni/ PS/Si Hydrogen Fuel cells. *Aspects in Mining & Mineral Science*, **11(2)**.

74. Zhang, D., She, F., Chen, J., Wei, L. and Li, H. (n.d.) Why Do Weak-Binding M-N-C Single-Atom Catalysts Still Possess Anomalously High Oxygen Reduction Activity in Alkaline Media?

75. Singh, R. K., Douglin, J. C., Jiang, L., Yassin, K., Brandon, S. and Dekel, D. R. (2023) CoOx-Fe3O4/N-rGO Oxygen Reduction Catalyst for Anion-Exchange Membrane Fuel Cells. *Energies*, **16(8)**.

76. Han, L. and Galán-Mascarós, J. R. (2020) The positive effect of iron doping in the electrocatalytic activity of cobalt hexacyanoferrate. *Catalysts*, **10(1)**.

77. Song, R., Han, J., Okugawa, M., Belosludov, R., Wada, T., Jiang, J., Wei, D., Kudo, A., Tian, Y., Chen, M. and Kato, H. (2022) Ultrafine nanoporous intermetallic catalysts by high-temperature liquid metal dealloying for electro-chemical hydrogen production. *Nature Communications*, **13(1)**.

78. Saidi, W. A., Nandi, T. and Yang, T. (2023) Designing multinary noble metal-free catalyst for hydrogen evolution reaction. *Electrochemical Science Advances*, **3(6)**.

79. Song, Z., Li, J., Zhang, Q., Li, Y., Ren, X., Zhang, L. and Sun, X. (2023) Progress and perspective of single-atom catalysts for membrane electrode assembly of fuel cells. *Carbon Energy*, **5(7)**.

80. Yang, Y., Huang, M., Gao, B., Wang, C., Wu, H., Yuan, Y. and Zheng, J. (2025) Preparation of Fe, Co, Ni-based single atom catalysts, and the progress of their application in electrocatalysis. *Microstructures*, **5(1)**.

81. Luis-Sunga, M., Regent, L., Pastor, E. and García, G. (2020) Non-Precious Metal Graphene-Based Catalysts for Hydrogen Evolution Reaction. *Electrochem*, **1(2)**.

82. Tao, J., Wang, X., Xu, M., Liu, C., Ge, J. and Xing, W. (2023) Non-noble metals as activity sites for ORR catalysts in proton exchange membrane fuel cells (PEMFCs). *Industrial Chemistry & Materials*, **1(3)**.

83. Chen, T. W., Kalimuthu, P., Veerakumar, P., Lin, K. C., Chen, S. M., Ramachandran, R., Mariyappan, V. and Chitra, S. (2022) Recent Developments in Carbon-Based Nanocomposites for Fuel Cell Applications: A Review. *Molecules*, **27(3)**.

84. Liu, J. and Zhang, T. (2024) Design of Membrane Electrode Assembly with Non-precious Metal Catalyst for Self-humidifying Proton Exchange Membrane Fuel Cell. *Springer Proceedings in Physics*, **393**, 401–411.

85. Santori, P. G., Mondal, A. N., Dekel, D. R. and Jaouen, F. (2020) The critical importance of ionomers on the electrochemical activity of platinum and platinum-free catalysts for anion-exchange membrane fuel cells. *Sustainable Energy and Fuels*, **4(7)**, 3300–3307.

86. Mondelli, C., Gözaydin, G., Yan, N. and Pérez-Ramírez, J. (2020) Biomass valorisation over metal-based solid catalysts from nanoparticles to single atoms. *Chemical Society Reviews*, **49(12)**, 3764–3782.

87. Silva, J., Rocha, C., Soria, M. A. and Madeira, L. M. (2022) Catalytic Steam Reforming of Biomass-Derived Oxygenates for H_2 Production: A Review on Ni-Based Catalysts. *ChemEngineering*, **6(3)**.

88. Zhao, W., Xu, D., Chen, Y., Cheng, J., You, C., Wang, X., Dong, S., Tao, Q. and Zhu, P. (2022) Surface Modification towards Integral Bulk Catalysts of Transition Metal Borides for Hydrogen Evolution Reaction. *Catalysts*, **12(2)**.

89. Mo, X., Bouchet Fabre, B., Herlin-Boime, N. and Tse, E. C. M. (2023) Rapid laser synthesis of surfactantless tantalum-based nanomaterials as bifunctional catalysts for direct peroxide–peroxide fuel cells. *SmartMat*, **4(6)**.

90. Wei, J., Xu, L., Hu, L., Wang, T. and Ma, Y. (2023) Dual-Doping Strategy for Enhancing Hydrogen Evolution on Molybdenum Carbide Catalysts. *Catalysts*, **13(6)**.

91. Zhou, M., Jiang, X., Kong, W., Li, H., Lu, F., Zhou, X. and Zhang, Y. (2023) Synergistic Effect of Dual-Doped Carbon on Mo_2C Nanocrystals Facilitates Alkaline Hydrogen Evolution. *Nano-Micro Letters*, **15(1)**.

92. Zhang, L., Fan, L., Yang, P., Li, M., Zhang, H., Tang, Y., Kang, Z., Guo, H., Wang, R. and Sun, D. (2020) Green synthesis of hierarchical carbon coupled with Fe_3O_4/Fe_2C as an efficient catalyst for the oxygen reduction reaction. *Materials Advances*, **1(6)**, 2010–2018.

93. Pander, M., Gil-San-Millan, R., Delgado, P., Perona-Bermejo, C., Kostrzewa, U., Kaczkowski, K., Kubicki, D. J., Navarro, J. A. R. and Bury, W. (2023) MOF/polymer hybrids through in situ free radical polymerization in metal-

organic frameworks. *Materials Horizons*, **10(4)**, 1301–1308.

94. Dutt, S., Kumar, A. and Singh, S. (2023) Synthesis of Metal Organic Frameworks (MOFs) and Their Derived Materials for Energy Storage Applications. *Clean Technologies*, **5(1)**, 140–166.

95. Duan, J., Chen, S. and Zhao, C. (2017) Ultrathin metal-organic framework array for efficient electrocatalytic water splitting. *Nature Communications*, **8**.

96. Tang, Y. (2024) Covalent Organic Framework Composites for Catalysis: Opportunities and Challenges. *Highlights in Science, Engineering and Technology ESMA*, *Vol. 2024*.

97. Lalawmpuia, R., Lalhruaitluangi, M., Lalhmunsiama and Tiwari, D. (2024) Metal organic framework (MOF): Synthesis and fabrication for the application of electrochemical sensing. *Environmental Engineering Research*, **29(5)**.

98. Kumar, G. (2024) MOF-based Heterogeneous Catalysis: A Frontier in Sustainable Chemical Transformations. *Catalysis Research*, **04(04)**, 1–5.

99. Bhattacharyya, S., Das, C. and Maji, T. K. (2018) MOF derived carbon nanocomposite materials as efficient electrocatalysts for oxygen reduction and oxygen and hydrogen evolution reactions. *RSC Advances*, **8(47)**, 26728–26754.